



An investigation into the processes controlling the global distribution of dissolved ^{231}Pa and ^{230}Th in the ocean and the sedimentary $^{231}\text{Pa}/^{230}\text{Th}$ ratios by using an ocean general circulation model COCO ver4.0

5

Yusuke Sasaki¹, Hidetaka Kobayashi¹, and Akira Oka¹

¹ Atmosphere and Ocean Research Institute, The University of Tokyo, Kashiwa, Japan

Correspondence to: Akira Oka (akira@aori.u-tokyo.ac.jp)

Abstract. Sedimentary $^{231}\text{Pa}/^{230}\text{Th}$ ratios provide clues to estimate the strength of past ocean circulation. For its estimation, understanding the processes controlling the distributions of dissolved ^{231}Pa and ^{230}Th in the ocean is important. However, simulations of dissolved and particulate ^{231}Pa and ^{230}Th in the modern ocean, recently obtained from the GEOTRACES project, remain challenging. Here we show an improved model simulation of ^{231}Pa and ^{230}Th in the global ocean by introducing bottom scavenging and the dependence of scavenging efficiency on particle concentration with water-column reversible scavenging. The incorporation of bottom scavenging improves the simulated distribution of dissolved ^{231}Pa and ^{230}Th in the deep ocean, which has been overestimated in models not considering the bottom scavenging. We further demonstrate that introducing the dependence of scavenging efficiency on particle concentration results in a high concentration of dissolved ^{230}Th in the Southern Ocean. Our best simulation can well reproduce not only the oceanic distribution of ^{231}Pa and ^{230}Th but also the sedimentary $^{231}\text{Pa}/^{230}\text{Th}$ ratios. Sensitivity analysis reveals that oceanic advection of ^{231}Pa primarily determines sedimentary $^{231}\text{Pa}/^{230}\text{Th}$ ratios. On the other hand, ^{230}Th advection and bottom scavenging have an opposite effect to ^{231}Pa advection on the sedimentary $^{231}\text{Pa}/^{230}\text{Th}$ ratios, reducing their latitudinal contrast. Our model realistically simulates the residence times of ^{231}Pa and ^{230}Th , whereas previous models that reported the similar distribution of sedimentary $^{231}\text{Pa}/^{230}\text{Th}$ ratios significantly overestimate the residence times for both ^{231}Pa and ^{230}Th .

1 Introduction

The $^{231}\text{Pa}/^{230}\text{Th}$ ratios in marine sediments are used for estimating past ocean circulation strength (Böhm et al., 2015; Gherardi et al., 2009; McManus et al., 2004; Yu et al., 1996). Alpha decay of ^{235}U and ^{234}U produces ^{231}Pa (half-life of ~ 32.5 kyr) and ^{230}Th (half-life of ~ 75.2 kyr), respectively, at an approximately constant ratio of 0.093 in the ocean (Henderson and Anderson, 2003). ^{231}Pa and ^{230}Th are absorbed onto and desorbed from the surfaces of sinking particles (reversible scavenging; Bacon and Anderson, 1982) and eventually removed from the water column into marine sediments.



Differential scavenging efficiencies of ^{231}Pa and ^{230}Th result in differences in their residence times in the ocean. The residence time of ^{231}Pa and ^{230}Th was estimated at 111 years and 26 years, respectively (Yu et al., 1996). The shorter residence time of ^{230}Th indicates that ^{230}Th generated from ^{234}U is removed relatively quickly to marine sediments. On the other hand, the longer residence time of ^{231}Pa indicates that ^{231}Pa produced from ^{235}U is transported for a longer period by ocean advection and mixing. Therefore, the deviation of the sedimentary $^{231}\text{Pa}/^{230}\text{Th}$ ratios from the constant production ratio of 0.093 has been used as a proxy for ocean circulation (Yu et al., 1996). For example, the sedimentary $^{231}\text{Pa}/^{230}\text{Th}$ ratios from the Bermuda Rise were closer to 0.093 at the Last Glacial Maximum (LGM) than today, which suggests that the Atlantic meridional overturning circulation (AMOC) was weaker at the LGM (McManus et al., 2004; Böhm et al., 2015).

To use the sedimentary $^{231}\text{Pa}/^{230}\text{Th}$ ratios as a proxy for ocean circulation in a more quantitative manner, one needs to take into account the different scavenging efficiencies of different marine particle types (e.g., organic carbon, calcite, and opal) as well as the distribution of these particles (Chase et al., 2002; Edwards et al., 2005). Sinking particles effectively scavenge ^{231}Pa and ^{230}Th in regions with high particle concentrations. In general, ^{231}Pa has a longer residence time than ^{230}Th , because sinking particles scavenge ^{230}Th more strongly. However, as for opal particles, Chase et al. (2002) argue that opal scavenges ^{231}Pa more effectively than ^{230}Th . This report is consistent with observational studies that find high $^{231}\text{Pa}/^{230}\text{Th}$ ratios in the Southern Ocean, where opal sinking flux is high (Chase et al., 2003).

Authors of previous modeling studies have tried to simulate the global distributions of ^{231}Pa and ^{230}Th (Dutay et al., 2009; Gu and Liu, 2017; Henderson et al., 1999; Marchal et al., 2000; Rempfer et al., 2017; Siddall et al., 2005; van Hulst et al., 2018). There are also modeling studies that discuss the relationship between the strength of the AMOC and changes in sedimentary $^{231}\text{Pa}/^{230}\text{Th}$ ratios (Missiaen et al., 2020a; Missiaen et al., 2020b; Siddall et al., 2007). Siddall et al. (2005) pioneered the three-dimensional (3D) simulation of both ^{231}Pa and ^{230}Th by incorporating reversible scavenging. Their control simulation appropriately reproduced the observed distribution of sedimentary $^{231}\text{Pa}/^{230}\text{Th}$ ratios; it showed high sedimentary $^{231}\text{Pa}/^{230}\text{Th}$ ratios in regions where the sinking opal particle flux is high. In their control simulation, the concentrations of dissolved ^{231}Pa and ^{230}Th increased linearly with depth; this pattern agreed broadly with observed features. However, simulated dissolved ^{231}Pa and ^{230}Th were both higher than observations in the deep ocean. In addition to reversible scavenging by sinking ocean particles, several studies (e.g., Roy-Barman, 2009; Okubo et al., 2012) have pointed out the importance of additional scavenging at the seafloor (bottom scavenging) and the continental boundaries (boundary scavenging). Rempfer et al. (2017) used a 3D ocean model of intermediate complexity similar to that used by Siddall et al. (2005) and reproduced the distributions of dissolved ^{231}Pa and ^{230}Th more realistically by introducing bottom scavenging and boundary scavenging. On the other hand, Henderson et al. (1999) reproduced the distribution of dissolved ^{230}Th in their ocean general circulation model (OGCM) simulation by changing the efficiency of reversible scavenging depending on particle concentration. Several OGCM studies have tried to simulate the distributions of ^{231}Pa and ^{230}Th (e.g., Dutay et al., 2009; Gu and Liu, 2017). However, these studies also overestimated the concentrations of dissolved ^{231}Pa and ^{230}Th in the deep ocean, as in Siddall et al. (2005). Although previous modeling studies well reproduced the observed distribution of sedimentary $^{231}\text{Pa}/^{230}\text{Th}$ ratios, further studies are required for more quantitative understanding of the processes that control



their global distribution. Recently, the GEOTRACES project has led to a dramatic increase in the number of observations of dissolved and particulate ^{231}Pa and ^{230}Th . The GEOTRACES database provides an opportunity to test models describing the cycling of these two radioisotopes in the global ocean. This study reports the results of our OGCM simulations, which reproduce dissolved ^{231}Pa and ^{230}Th more realistically than previous simulations by introducing bottom scavenging and the dependence of scavenging efficiency on particle concentration. Furthermore, we quantitatively discuss the processes that control the global distribution of sedimentary $^{231}\text{Pa}/^{230}\text{Th}$ ratios; by performing a series of sensitivity simulations, we clarify how the individual processes (i.e., water-column reversible scavenging, ocean transport, and bottom scavenging) affect the global distribution of dissolved ^{231}Pa and ^{230}Th and sedimentary $^{231}\text{Pa}/^{230}\text{Th}$ ratios.

2 Materials and Methods

2.1 Ocean general circulation model

The OGCM used in this study is COCO version 4.0 (Hasumi, 2006), the ocean component of the coupled ocean-atmosphere general circulation model MIROC version 3.2 (K-1 Model Developers, 2004). The COCO is also used as the ocean part of MIROC earth system model (Hajima et al. 2020; Ohgaito et al., 2021). The model domain is global, with about one-degree horizontal resolution and 43 vertical layers. Surface boundary conditions are given from monthly averages of zonal and meridional components of wind stress, air temperature, specific humidity, net shortwave radiation, downward longwave radiation, freshwater flux, air pressure, and wind speed. These boundary conditions are taken from the output of a pre-industrial simulation with MIROC (Kobayashi et al., 2015; Oka et al., 2012). To calculate ^{231}Pa and ^{230}Th , we perform offline tracer simulation using physical fields obtained in advance by COCO (Oka et al., 2008, 2009). The tracer model is integrated for 3,000 years, by which time tracer fields reach a steady state. We analyze the average of the last 100 years of the integration.

The physical fields used in this study is based on MIROC climate model simulations, and its reproducibility has been discussed and confirmed in a variety of literature (e.g., K-1 Model Developers, 2004; Gregory et al., 2005; Oka et al., 2006; Stouffer et al., 2006). We also note that the physical fields used are the same as PI simulation reported in Kobayashi et al. (2015) and Kobayashi and Oka (2018).

2.2 Particle fields

Following Siddall et al. (2005), the distribution of biogenic particles (organic carbon, calcite, and opal) is used to evaluate the scavenging of both ^{231}Pa and ^{230}Th . We define the concentration M of each particle type [g m^{-3}] as $M = F/w_s$, where F is the particle flux [$\text{g m}^{-2} \text{yr}^{-1}$] and w_s is the constant settling velocity [m yr^{-1}]. The vertical particle flux is calculated using the export flux from the euphotic zone and an assumed vertical profile of each particle type. The detailed procedure is explained below.



First, the particulate organic carbon (POC) export flux from the euphotic zone is calculated by multiplying the distribution of primary production derived from satellite observations (Behrenfeld and Falkowski, 1997) by the export ratio (Dunne et al., 2005). From POC export flux and $M = F/w_s$, the concentration of POC at the base of the euphotic zone, $M_{\text{POC}}(z_0)$, where z_0 is the depth of the bottom of the euphotic zone, is obtained. After obtaining $M_{\text{POC}}(z_0)$, the POC concentration in the water column is expressed (Marchal et al., 1998) as

$$M_{\text{POC}} = M_{\text{POC}}(z_0) \left(\frac{z}{z_0}\right)^{-\varepsilon}, \quad (1)$$

where ε is a remineralization exponent for POC.

Next, the calcite and opal export fluxes from the euphotic zone are calculated by multiplying the POC export flux by their rain ratios, which are estimated following formulations of Siddall et al. (2005) and Maier-Reimer (1993); please refer to Eq. (2)–(5) of Siddall et al. (2005) for detail. The calcite particle concentration is calculated by assuming an exponentially decreasing vertical profile (Henderson et al., 1999; Marchal et al., 2000; Siddall et al., 2005). Thus, we have

$$M_{\text{CaCO}_3} = M_{\text{CaCO}_3}(z_0) \exp\left(\frac{z_0 - z}{z_p}\right), \quad (2)$$

where z_p is the calcite penetration depth. While the opal concentration is expressed as an exponentially decreasing vertical profile in some previous studies (e.g., Henderson et al., 1999), we consider opal dissolution to be dependent on temperature, following Siddall et al. (2005), as

$$M_{\text{opal}} = M_{\text{opal}}(z_0) \exp\left[\frac{D_{\text{opal}}(z_0 - z)}{w_s}\right], \quad (3a)$$

$$D_{\text{opal}} = B(T - T_0), \quad (3b)$$

where D_{opal} [yr^{-1}] is the opal dissolution rate, T_0 is the minimum temperature [$^{\circ}\text{C}$] of seawater in the model, and B is a dissolution constant [$^{\circ}\text{C}^{-1} \text{yr}^{-1}$]. Table 1 lists the parameter values used in this study. Figure S10 shows particle fluxes in the surface ocean.

2.3 Reversible scavenging model

We use a tracer model of ^{231}Pa and ^{230}Th based on Siddall et al. (2005). The dissolved concentration (A_d) and particle concentration (A_p) of ^{231}Pa and ^{230}Th are calculated from the following equations:

$$\frac{\partial A_{\text{total}}^i}{\partial t} = \beta^i - \lambda^i A_{\text{total}}^i - w_s \frac{\partial A_p^i}{\partial z} + \text{Transport}, \quad (4a)$$

$$A_{\text{total}}^i = A_p^i + A_d^i. \quad (4b)$$

In Eq. (4a), the first term on the right-hand side (β^i) represents production from uranium (^{231}Pa from ^{235}U ; ^{230}Th from ^{234}U), the second term represents radioactive decay, the third term represents the effect of vertical particle settling, and the fourth term represents ocean transport by advection, diffusion, and convection. The superscript i represents the isotope type (^{231}Pa , ^{230}Th).



By following a reversible scavenging model (Bacon and Anderson, 1982), the relationship between the radionuclide concentration in the dissolved phase (A_d) and particulate phase (A_p) is represented by the partition coefficient (K_j^i) as

$$A_p^i = \sum_j A_{j,p}^i, \quad (5a)$$

125

$$K_j^i = \frac{A_{j,p}^i}{A_d^i \cdot C_j}, \quad (5b)$$

where subscript j represents the particle type (organic carbon, calcite, opal) and C_j is the dimensionless ratio of particle concentration to the density of seawater. The formulation of the reversible scavenging was also described in Oka et al., (2009, 2021) and readers can obtain its detail description therein. The partition coefficient depends on the type of particles (Siddall et al., 2005). The partition coefficients of ^{231}Pa and ^{230}Th for each type of particle have been estimated in previous studies (Luo and Ku, 1999; Chase et al., 2002). Chase et al. (2002) show that opal scavenges ^{231}Pa more efficiently than ^{230}Th , whereas calcite scavenges ^{230}Th more efficiently than ^{231}Pa . Here we use partition coefficients following Chase and Anderson (2004), as in other previous modeling studies (Dutay et al., 2009; Gu and Liu, 2017; Siddall et al., 2005; Table 2).

130

2.4 One-dimensional reversible scavenging model

In addition to the three-dimensional tracer model based on the OGCM, we use a simple, vertical, one-dimensional model to analyze simulation results in Section 4. In the one-dimensional model, we assume a steady state and ignore the effect of ocean transport in Eq. (4a). Furthermore, we do not take the radioactive decay term into account because it is much smaller than the production term. Under these assumptions, Eq. (4a) becomes

135

$$\beta^i - w_s \frac{\partial A_p^i}{\partial z} = 0. \quad (6)$$

In this one-dimensional model, production by uranium radioactive decay (the first term on the left side of Eq. (6)) is balanced by vertical transport through particle settling (the second term on the left side of Eq. (6)). If we assume that A_p^i is zero at the sea surface ($z = 0$), then Eq. (6) can be solved, leading to

140

$$A_p^i = \frac{\beta^i}{w_s} \cdot z. \quad (7)$$

From Eq. (5), we have

$$A_p^i = \sum_j A_{j,p}^i = (K_{\text{CaCO}_3}^i \cdot C_{\text{CaCO}_3} + K_{\text{opal}}^i \cdot C_{\text{opal}} + K_{\text{POC}}^i \cdot C_{\text{POC}}) \cdot A_d^i$$

145

$$= \sum_j (K_j^i \cdot C_j) \cdot A_d^i. \quad (8)$$

The dissolved concentration can be obtained from Eq. (7) and (8):

$$\begin{aligned} A_d^i &= \frac{1}{\sum_j (K_j^i \cdot C_j)} A_p^i \\ &= \frac{1}{\sum_j (K_j^i \cdot C_j)} \frac{\beta^i}{w_s} \cdot z. \quad (9) \end{aligned}$$



Equation (9) shows that the vertical profile of A_d^i is determined only by the particle settling speed, the partition coefficients, and the concentrations of each particle. By comparing results from the one-dimensional model and the three-dimensional tracer model, we can isolate the influence of ocean transport (i.e., advection, diffusion, and convection) on the simulated distributions of dissolved ^{231}Pa and ^{230}Th (see Section 4; Table 3).

2.5 Experimental design

This study conducts a series of OGCM experiments. First, we perform an experiment named Siddall_EXP using the same parameters and formulations as in Siddall et al. (2005).

Second, we perform an experiment named BTM_EXP, in which we additionally take bottom scavenging into account. In BTM_EXP, we assume a globally uniform concentration of lithogenic particles in the deepest layer of the OGCM, following Rempfer et al. (2017). The intensity of the bottom scavenging depends on two parameters: the partition coefficient for lithogenic particles (K_{bottom}) and the concentration of lithogenic particles (C_{bottom}). The value of C_{bottom} is taken from Rempfer et al. (2017): $C_{\text{bottom}} = 6.0 \times 10^{-8} \text{ g cm}^{-3}$. This value is within the range of values from 4.0×10^{-8} to $1.65 \times 10^{-6} \text{ g cm}^{-3}$ observed in the benthic nepheloid layers (50-130 m above the bottom) in the North Atlantic as reported by Lam et al. (2015). By varying K_{bottom} , we perform a number of simulations with different bottom scavenging intensities.

Third, we perform a sensitivity experiment named KREF_EXP concerned with the reference partition coefficient (K_{ref}). In KREF_EXP, in addition to varying the partition coefficient for lithogenic particles (K_{bottom}), we also vary the reference partition coefficients (K_{ref}) from the values assumed in Siddall_EXP and BTM_EXP.

Finally, we perform an experiment named PCE_EXP, in which we incorporate the dependence of scavenging efficiency on particle concentration. In PCE_EXP, K_{ref} is not assumed to be constant but varies according to the following formulation of Henderson et al. (1999):

$$K_{\text{ref}} = \left(\frac{C_{\text{total}}}{C_{\text{ref}}} \right)^{-0.42} \times 10^7, \quad (10)$$

where C_{total} [g cm^{-3}] is the total concentration of all sinking particles ($C_{\text{total}} = C_{\text{CaCO}_3} + C_{\text{opal}} + C_{\text{POC}}$) and C_{ref} [g cm^{-3}] is the reference concentration. Due to the dependence of K_{ref} on C_{total} , the scavenging efficiency becomes lower under higher particle concentrations and higher under lower particle concentrations. We conduct several simulations by varying C_{ref} between 10^{-9} and $10^{-6} \text{ g cm}^{-3}$. Although the observed decrease of the partition coefficient with increased bulk particle concentration is not entirely understood (Pavia et al., 2018), we will show that this particle concentration effect becomes essential for controlling dissolved ^{230}Th in some ocean regions.



3 Results

3.1 Dissolved ^{231}Pa and ^{230}Th along the Atlantic meridional transects

First, we discuss the results of Siddall_EXP, focusing on the meridional distribution of ^{231}Pa and ^{230}Th in the Atlantic Ocean. Figure 1 shows the dissolved concentrations of ^{231}Pa and ^{230}Th simulated in Siddall_EXP along the Atlantic transect, together with GEOTRACES data (see Fig. S1 for the location of observations referenced in this study). We confirm that the distributions of dissolved ^{231}Pa and ^{230}Th in Siddall_EXP are approximately the same as those reported in Siddall et al. (2005; their Fig. 2). Because ^{231}Pa and ^{230}Th exchange reversibly with sinking particles and are transported to the deep ocean, the dissolved ^{231}Pa and ^{230}Th concentrations increase with depth, both in the model simulation and in observations. However, as in Siddall et al. (2005), the model simulation overestimates dissolved ^{231}Pa and ^{230}Th concentrations at depths greater than 2,000 m and 1,000 m, respectively. For quantitative analysis, we perform a linear regression analysis between the simulation results and observed data from the GEOTRACES GA02 transect; we calculate the root mean square deviation (RMSD), the correlation coefficient (R), and the slope of the linear regression (s) of modeled activity versus measured activity, as summarized in Table S1. The linear regression line slope indicates the model's ability to reproduce the observed distribution; it approaches 1.0 when the model simulation realistically reproduces the target distribution (Dutay et al., 2009; Gu and Liu, 2017). For Siddall_EXP, the slope of linear regression line is significantly larger than 1.0 for both ^{231}Pa (s=1.88, R=0.72 and RMSD=0.15) and ^{230}Th (s=4.44, R=0.89 and RMSD=1.31; Table S1). This overestimation is also found in other previous model simulations (e.g., Dutay et al., 2009; Gu and Liu, 2017).

Next, to reduce the overestimation of the simulated concentrations in the deep ocean, we additionally incorporate bottom scavenging in benthic nepheloid layers (BTM_EXP). The dissolved ^{231}Pa and ^{230}Th distributions are shown in Fig. 2 and 3, respectively. As expected, the incorporation of bottom scavenging helps reduce ^{231}Pa and ^{230}Th concentrations in the deep ocean, improving the model's agreement with the data. This result is consistent with a recent model study of Rempfer et al. (2017). As for the distribution of dissolved ^{231}Pa , the model results come relatively close to the GEOTRACES data if $K_{\text{bottom}}^{\text{Pa}}$ is set equal to 5.0×10^5 (s=1.04, R=0.90 and RMSD=0.05; see CTRL_EXP in Table S1; Fig. 2c and 2d). On the other hand, it is difficult to reproduce the observed distribution of dissolved ^{230}Th in BTM_EXP. With $K_{\text{bottom}}^{\text{Th}} = 1.0 \times 10^6$, the concentrations of ^{230}Th in bottom waters come close to observed values (Fig. 3c and 3d), but the concentrations in the deep ocean (from 2000 m to 5000 m) remain overestimated. In the case of larger $K_{\text{bottom}}^{\text{Th}}$, the simulated ^{230}Th concentrations approach observed values in the deep ocean but are significantly lower than measurements in bottom waters (e.g., $K_{\text{bottom}}^{\text{Th}} = 1.0 \times 10^7$ in Fig. 3g and 3h). These results indicate that considering bottom scavenging alone is not sufficient for accurately simulating ^{230}Th distribution in our model, even though bottom scavenging is an important process controlling ^{230}Th distribution (Lerner et al., 2020). In the following experiments (i.e., KREF_EXP and PCE_EXP), we focus solely on ^{230}Th .

To reproduce the distribution of ^{230}Th more realistically, we change the value of the reference partition coefficient ($K_{\text{ref}}^{\text{Th}}$) in addition to $K_{\text{bottom}}^{\text{Th}}$ (KREF_EXP). Figure 4 summarizes the results of KREF_EXP and shows the simulated vertical



distributions of dissolved ^{230}Th for various values of $K_{\text{ref}}^{\text{Th}}$ and $K_{\text{bottom}}^{\text{Th}}$ (see Fig. 4g). Note that, for example, the simulation
210 R2_B5 means that $K_{\text{ref}}^{\text{Th}}$ is set to 2.0×10^7 and $K_{\text{bottom}}^{\text{Th}}$ to 5.0×10^5 . In the cases where $K_{\text{bottom}}^{\text{Th}}$ is set to 5.0×10^5 (namely
R2_B5, R4_B5, and R6_B5), the ^{230}Th concentrations systematically change depending on $K_{\text{ref}}^{\text{Th}}$; as the reversible scavenging
on sinking particles becomes stronger (i.e., for larger $K_{\text{ref}}^{\text{Th}}$), the concentrations of dissolved ^{230}Th become smaller throughout
the water column (Fig. 4c, 4e, and 4f). As discussed for BTM_EXP, it is also confirmed that the stronger bottom scavenging
(i.e., larger $K_{\text{bottom}}^{\text{Th}}$), the lower the concentrations near the sea bottom (e.g., see R2_B5, R2_B10, and R2_B20). For some
215 combinations of water-column scavenging and bottom scavenging, simulations (e.g., R6_B5, R4_B5, R4_B10) reasonably
reproduce the observed profile of dissolved ^{230}Th concentration. Among our KREF_EXP simulations, the R6_B5 simulation
(Fig. 4f) shows the slope of the linear regression line nearest to 1.0 ($s=0.88$, $R=0.81$, and $\text{RMSD}=0.20$; Table S1) where $K_{\text{ref}}^{\text{Th}}$
is higher ($K_{\text{ref}}^{\text{Th}} = 6.0 \times 10^7$) than for Siddall_EXP and BTM_EXP ($K_{\text{ref}}^{\text{Th}} = 1.0 \times 10^7$). In the R6_B5 simulation (Fig. 4f),
the vertical profile of dissolved ^{230}Th is significantly improved from that of Siddall_EXP (Fig. 1d) and BTM_EXP (Fig. 3).
220 We confirmed that the R6_B5 simulation captures the observed features of the Atlantic transects of the GEOTRACES data
(Fig. 5a). However, the R6_B5 simulation still underestimates the concentrations of dissolved ^{230}Th from the surface to
intermediate depths (see Fig. 4f). Also, the high concentrations of dissolved ^{230}Th observed in the Southern Ocean in
GEOTRACES data are not well reproduced (Fig. 5a). To address this issue, we performed additional simulations by slightly
changing the values of $K_{\text{ref}}^{\text{Th}}$ and $K_{\text{bottom}}^{\text{Th}}$ from the R6_B5 simulation (not shown), but found that it is difficult to remove the
225 preceding deficiencies by merely changing the values of $K_{\text{ref}}^{\text{Th}}$ and $K_{\text{bottom}}^{\text{Th}}$ in KREF_EXP.

Finally, we discuss PCE_EXP, in which the dependence of scavenging efficiency on particle concentration is taken
into account, according to Eq. (10). We conduct several simulations by varying the value of the reference concentration
(C_{ref}) between 10^{-9} and 10^{-6} g cm^{-3} . Among these results, we here discuss the case with $C_{\text{ref}} = 10^{-7}$ g cm^{-3} , which shows
the best agreement with observations. Compared to the case in which the dependence of scavenging efficiency on particle
230 concentration is not considered (i.e., R6_B5 simulation of KREF_EXP), PCE_EXP is expected to show smaller (larger) $K_{\text{ref}}^{\text{Th}}$
for the higher (lower) concentration of sinking particles. In Fig. 5, we compare the simulated dissolved ^{230}Th distribution
obtained from PCE_EXP and R6_B5 simulation of KREF_EXP. Owing to the dependence of scavenging efficiency on
particle concentration, PCE_EXP reproduces the vertical distribution of dissolved ^{230}Th slightly better than KREF_EXP (Fig.
5d). The regression analysis also confirms that the agreement with the GEOTRACES data becomes improved in PCE_EXP
235 ($s=0.98$ and $R=0.84$; CTL_EXP in Table S1). It is worthy to note that the distribution in the Southern Ocean is significantly
improved in PCE_EXP (Fig. 5b) compared to KREF_EXP (Fig. 5a) as a result of the non-uniform distribution of the
reference partition coefficient $K_{\text{ref}}^{\text{Th}}$ (Fig. 5c). In the Southern Ocean, where particle concentration is relatively higher than in
other regions (Honjo et al., 2008), the value of $K_{\text{ref}}^{\text{Th}}$ in PCE_EXP is lower than that in the R6_B5 simulation of KREF_EXP
($K_{\text{ref}}^{\text{Th}} = 6 \times 10^7$; i.e., $\log_{10} K_{\text{ref}}^{\text{Th}} \sim 7.8$) (Fig. 5c). Therefore, the concentration of dissolved ^{230}Th in PCE_EXP becomes
240 high compared to the KREF_EXP, thereby more realistically reproduces the distribution of dissolved ^{230}Th in the Southern



Ocean. Hereafter, our best simulation (i.e., $K_{\text{bottom}}^{Pa} = 5.0 \times 10^5$ case of BTM_EXP for ^{231}Pa and PCE_EXP for ^{230}Th) is called CTRL_EXP (see Table 2 for parameter values of CTRL_EXP).

3.2 Reproducibility along GEOTRACES GA03 and GP16 transects

So far, we have compared our model results with observations mainly from the Atlantic meridional GEOTRACES
245 transects (i.e., GA02 and GIPY05). Here, we will compare our CTRL_EXP with other available GEOTRACES transects of
GA03 in the subtropical North Atlantic (Hayes et al., 2015) and GP16 in the South Pacific (Pavia et al., 2018).

Figure S5 shows the results of CTRL_EXP along with the GEOTRACES GA03 data. For dissolved ^{231}Pa , a high
concentration is found at a depth of about 3000 m and has a maximum on the eastern side of the basin from the
GEOTRACES data (Fig. S5a). The model also reproduces a high concentration around 3000 m, but its maximum is
250 somewhat smaller than observations and is located not on the eastern side but the western side of the basin. Similar features
are also found for dissolved ^{230}Th (Fig. S5b). Interestingly, observed particulate ^{231}Pa and ^{230}Th concentrations are relatively
well reproduced by the model (Fig. S5c and S5d), but localized high concentration near the sea bottom found in
GEOTRACES data is not well captured in the model. Our model may not sufficiently reproduce the bottom and boundary
scavenging associated with terrestrial particles in this region. More sophisticated treatment of bottom and boundary
255 scavenging might be required for addressing these issues.

Figure S6 shows the results of CTRL_EXP along with the GEOTRACES GP16 data. As with the other section data,
CTRL_EXP approximately reproduces the distribution of ^{231}Pa and ^{230}Th . In this transect, the observational data shows a
clear signal associated with hydrothermal vents: low concentrations of dissolved ^{231}Pa and ^{230}Th and high concentrations of
particulate ^{231}Pa and ^{230}Th , which are not simulated in our model. Processes related to the hydrothermal vents are not
260 explicitly incorporated in the present ^{231}Pa and ^{230}Th model simulations; its detail treatment is beyond our scope but appears
necessary for more realistic simulations.

3.3 Particulate ^{231}Pa and ^{230}Th

By conducting a series of experiments described above, this study successfully reproduces the observed
distributions of dissolved ^{231}Pa and ^{230}Th , shown again in Fig. 6a and 6b, respectively. In addition to dissolved ^{231}Pa and
265 ^{230}Th , particulate ^{231}Pa and ^{230}Th simulated in CTRL_EXP are compared with the reported observations (Fig. 6c and 6d). In
addition to the GEOTRACES dataset, we use several reported observations here (i.e., data referenced in Siddall et al., 2005,
Marchal et al., 2007, and Lerner et al., 2020; namely, from Colley et al., 1995; Moran et al., 1997; Moran et al., 2001;
Rutgers van der Loeff and Berger, 1993; Vogler et al., 1998; Walter et al., 1997; Cochran et al., 1987; Moran et al., 2002;
Guo et al., 1995). The model captures the observed tendency that the concentration becomes higher in the high-latitude
270 Southern Ocean, as reported in previous studies (e.g., see Fig. 2 in Siddall et al. 2005). Although the number of available
observations is limited for the particulate phase, it is confirmed that our simulation reasonably reproduces observed
distributions for both dissolved and particulate phases.



3.4 Sedimentary $^{231}\text{Pa}/^{230}\text{Th}$ ratios

Our CTRL_EXP also well reproduces the global distribution of sedimentary $^{231}\text{Pa}/^{230}\text{Th}$ ratios (Fig. 6e) compared
275 with the reported observations (Mangianini & Sonntag, 1977; Muller & Mangini, 1980; Anderson et al., 1983; Shimmield et
al., 1986; Schmitz et al., 1986; Yang et al., 1986; Shimmield & Price, 1988; Yong Lao et al., 1992; François et al., 1993;
Frank et al., 1994; Frank, 1996; Bradtmiller et al., 2014, Luo et al., 2010, and their supplemental data). Sedimentary
 $^{231}\text{Pa}/^{230}\text{Th}$ ratios are high along the margin of the North Pacific and the North Atlantic, as well as in the Southern Ocean,
where particle concentrations are high. On the other hand, sedimentary $^{231}\text{Pa}/^{230}\text{Th}$ ratios are low in the low-latitude regions,
280 including subtropical gyres, where particle concentrations are low. These simulated features are consistent with observations
(circles in Fig. 6e). Siddall_EXP also reasonably reproduced the global distribution of sedimentary $^{231}\text{Pa}/^{230}\text{Th}$ ratios (Fig.
S4a, which will be discussed later). However, as shown above, the distributions of dissolved ^{231}Pa and ^{230}Th in the ocean are
significantly different between CTRL_EXP and Siddall_EXP. Thus, each experiment implies a different set of processes
controlling the distribution of sedimentary $^{231}\text{Pa}/^{230}\text{Th}$ ratios. We discuss these processes in the next section.

285 4 Discussion

4.1 Processes controlling sedimentary $^{231}\text{Pa}/^{230}\text{Th}$ ratios

This section focuses on our best simulation CTRL_EXP and discusses the processes controlling the global
distribution of sedimentary $^{231}\text{Pa}/^{230}\text{Th}$ ratios. For this purpose, we decompose the processes controlling sedimentary
 $^{231}\text{Pa}/^{230}\text{Th}$ ratios into three parts: water-column reversible scavenging, three-dimensional ocean transport, and bottom
290 scavenging. To evaluate how these three processes affect the distribution of $^{231}\text{Pa}/^{230}\text{Th}$ ratios, we conduct two additional
experiments (see Table 3). The first experiment is 3D_EXP, which is the same as CTRL_EXP except that bottom scavenging
is not taken into account (i.e., we set $K_{\text{bottom}}^{\text{Pa}} = K_{\text{bottom}}^{\text{Th}} = 0$ in 3D_EXP). The second is 1D_EXP, which is the one-
dimensional reversible scavenging model experiment described in Section 2.4. The tracer distribution in 1D_EXP is
determined solely by the one-dimensional vertical process of reversible scavenging; the strength of scavenging changes
295 spatially through changes in the partition coefficient (K_j^i of Eq. (9) in Section 2.4) that depends on the specified three-
dimensional particle concentration (C_j of Eq. (9)). By using results of CTRL_EXP, 3D_EXP, and 1D_EXP, we can extract
the influence of three processes: the influence of the one-dimensional vertical reversible scavenging is revealed by 1D_EXP,
the influence of bottom scavenging is revealed by the difference between CTRL_EXP and 3D_EXP, and the influence of
ocean transport is revealed by the difference between 3D_EXP and 1D_EXP. When we focus on sedimentary $^{231}\text{Pa}/^{230}\text{Th}$
300 ratios, each process described above can be further examined for ^{231}Pa and ^{230}Th individually. For example, the difference in
 $^{231}\text{Pa}/^{230}\text{Th}$ ratios between CTRL_EXP and 3D_EXP represents the influence of bottom scavenging of both ^{231}Pa and ^{230}Th ,
whereas the influence of bottom scavenging of ^{231}Pa alone can also be evaluated from CTRL_EXP and 3D_EXP (i.e.,
 $^{231}\text{Pa}(\text{CTRL})/^{230}\text{Th}(\text{3D})$ minus $^{231}\text{Pa}(\text{3D})/^{230}\text{Th}(\text{3D})$).



In 1D_EXP, the particulate concentration is obtained from Eq. (7); the particulate concentration increases linearly
305 with depth (Fig. S2c and S2d). The dissolved concentration is calculated from Eq. (9), suggesting that the concentration
becomes higher for a lower partition coefficient (K_j^i in Eq. (9)) and particle concentration (C_j in Eq. (9)). Mainly due to the
dependency on C_j , the dissolved concentration becomes higher (lower) in the area with lower (higher) particle concentration
in 1D_EXP. As a result, the dissolved concentration becomes very high in the deeper ocean, where the particle concentration
becomes lower for both ^{231}Pa and ^{230}Th (Fig. S2a and S2b). It is interesting to point out that the spatial pattern of dissolved
310 ^{231}Pa and ^{230}Th (Fig. S2a and S2b) is similar to that of K_{ref} in PCE_EXP (Fig. 5c) because both are affected by the amount
of particle concentration. More importantly, we emphasize here that the sedimentary $^{231}\text{Pa}/^{230}\text{Th}$ ratios in 1D_EXP become
uniform everywhere (0.093; Fig. S2e) because, as confirmed from Eq. (7), the ratio of particulate ^{231}Pa to particulate ^{230}Th
amounts everywhere to $\beta^{\text{Pa}}/\beta^{\text{Th}} = 0.093$, regardless of geographic location.

In 3D_EXP, three-dimensional ocean transport operates, in addition to water-column scavenging considered in
315 1D_EXP (Fig. S3). As described above, the influence of ocean transport can be evaluated from the difference between
3D_EXP and 1D_EXP (Fig. 7). On the other hand, the influence of bottom scavenging can be obtained from the difference
between CTL_EXP and 3D_EXP (Fig. 8). Note again that since the sedimentary $^{231}\text{Pa}/^{230}\text{Th}$ ratios in 1D_EXP are globally
uniform ($^{231}\text{Pa}/^{230}\text{Th} = 0.093$), their spatial distribution is not controlled by the one-dimensional vertical process of
scavenging alone, but varies with ocean transport. Figure 7e demonstrates that the ocean transport effect captures the overall
320 features of CTRL_EXP (Fig. 6e). On the other hand, bottom scavenging tends to cancel the effects of ocean transport and
weaken the spatial contrast of $^{231}\text{Pa}/^{230}\text{Th}$ ratios simulated in CTRL_EXP (Fig. 8e).

To evaluate the above processes controlling the sedimentary $^{231}\text{Pa}/^{230}\text{Th}$ ratios in more detail, we further decompose
the ocean transport contribution into those from ^{231}Pa and ^{230}Th , separately (Fig. 9a for ^{231}Pa and 9b for ^{230}Th). Similarly, we
further decompose the contribution of bottom scavenging into those for ^{231}Pa and ^{230}Th (Fig. 9c and 9d, respectively). In Fig.
325 9a, we demonstrate that ocean transport solely from ^{231}Pa (i.e., $^{231}\text{Pa}(3\text{D})/^{230}\text{Th}(1\text{D})$) can reproduce the overall distribution of
the sedimentary $^{231}\text{Pa}/^{230}\text{Th}$ ratios in CTRL_EXP (Fig. 6e). This result confirms that ocean transport of ^{231}Pa primarily
controls the distribution of sedimentary $^{231}\text{Pa}/^{230}\text{Th}$ ratios, consistent with previous studies (Yu et al., 1996; Marchal et al.,
2000). These previous studies suggest that the distribution of ^{231}Pa mainly determines the global distribution of sedimentary
 $^{231}\text{Pa}/^{230}\text{Th}$ ratios because the residence time of ^{231}Pa is longer than that of ^{230}Th .

330 Here, we further discuss how the ocean transport of ^{231}Pa controls the distribution of sedimentary $^{231}\text{Pa}/^{230}\text{Th}$ ratios.
Since changes in sedimentary ^{231}Pa correspond to particulate ^{231}Pa changes in the bottom ocean, we focus the ocean transport
effect on particulate ^{231}Pa (Fig. 7c). Consistent with Fig. 9a, Fig. 7c indicates that ocean transport acts to decrease (increase)
particulate ^{231}Pa in lower (higher) latitudes. We also found that particulate ^{231}Pa changes (Fig. 7c) are similar to those in
dissolved ^{231}Pa (Fig. 7a). Because most of ^{231}Pa are in the dissolved phase and ocean transport takes place mainly in the form
335 of dissolved ^{231}Pa , it is interpreted that ocean transport first controls the dissolved ^{231}Pa , and then the corresponding changes
in particulate ^{231}Pa take place so that the relationship between dissolved and particulate ^{231}Pa (i.e., Eq. (5b)) is satisfied.



Therefore, we need to focus on the processes that control the dissolved ^{231}Pa changes (Fig. 7a). As previously mentioned, in the case of no ocean transport (i.e., 1D_EXP), the dissolved ^{231}Pa concentration near the seabed in lower latitudes becomes very high (Fig. S2a). Ocean transport reduces high concentrations of dissolved ^{231}Pa in low latitude oceans by transporting
340 dissolved ^{231}Pa from lower latitudes to higher latitudes. At the same time, this ocean transport effect is also acting to particulate ^{231}Pa ; as a result, the ocean transport of ^{231}Pa causes lower sedimentary $^{231}\text{Pa}/^{230}\text{Th}$ ratios in lower latitudes and higher ratios in higher latitudes (Fig. 7e).

Contrary to ^{231}Pa , the influences of ^{230}Th transport on sedimentary $^{231}\text{Pa}/^{230}\text{Th}$ ratios have been usually regarded as small because ^{230}Th is generally assumed to be scavenged very quickly everywhere. However, our results demonstrate that
345 ocean transport of ^{230}Th also affects the distribution of sediment $^{231}\text{Pa}/^{230}\text{Th}$ to some extent. As a matter of course, ^{230}Th ocean transport acts in the opposite direction of ^{231}Pa ocean transport, reducing the spatial contrast in sedimentary $^{231}\text{Pa}/^{230}\text{Th}$ ratios (Fig. 9b). However, an exception is found in the Southern Ocean, where the ^{230}Th ocean transport contributes to higher sedimentary $^{231}\text{Pa}/^{230}\text{Th}$ ratios, in the same way as the ^{231}Pa ocean transport. Because opal scavenges ^{231}Pa more effectively than ^{230}Th (Chase et al., 2002), ^{231}Pa transported toward the Southern Ocean is expected to be immediately removed there
350 due to the high opal flux. Therefore, previous studies concluded that ocean transport of ^{231}Pa explains high sedimentary $^{231}\text{Pa}/^{230}\text{Th}$ ratios in the Southern Ocean. On the other hand, in addition to ocean transport of ^{231}Pa , our results suggest that ocean transport of ^{230}Th also contributes to the high $^{231}\text{Pa}/^{230}\text{Th}$ ratios in the Southern Ocean. This result implies that scavenging of ^{230}Th is not so efficient in the Southern Ocean as previously expected due to the dependence of scavenging efficiency on particle concentration. This interpretation is consistent with the high concentration of dissolved ^{230}Th in the
355 Southern Ocean (Fig. 6b).

Bottom scavenging promotes the removal of both ^{231}Pa and ^{230}Th near the seafloor and tends to cancel the influence of ocean transport. Namely, the bottom scavenging of ^{231}Pa reduces the contrast among sedimentary $^{231}\text{Pa}/^{230}\text{Th}$ ratios (Fig. 9c), whereas the bottom scavenging of ^{230}Th increases this contrast (Fig. 9d). Because the influences of bottom scavenging of ^{231}Pa tends to be stronger than that of ^{230}Th , bottom scavenging overall results in reducing the contrast of $^{231}\text{Pa}/^{230}\text{Th}$ ratios
360 (Fig. 8e). Precisely speaking, the actual processes of the bottom scavenging effect on the sedimentary ^{231}Pa and ^{230}Th appear somewhat complicated compared with those of the ocean transport effect. The effect of the bottom scavenging is two-fold. First, extra particles in the bottom ocean lead to an increase of sedimentary ^{231}Pa and ^{230}Th (e.g., positive values near the bottom in low latitudes in Fig. 8c). Second, the bottom scavenging removes ^{231}Pa and ^{230}Th from the ocean, which reduces the concentration of dissolved ^{231}Pa and ^{230}Th in the ocean interior (Fig. 8a and 8b). The changes in dissolved-phase concentration then lead to changes in particulate-phase concentration in a way such that the Eq. (5b) is satisfied. The former
365 leads to higher sedimentary ^{231}Pa and ^{230}Th , whereas the latter leads to lower sedimentary ^{231}Pa and ^{230}Th . Our results indicate that the former process becomes more critical than the latter in the low latitudes, and the sedimentary ^{231}Pa increases. In contrast, the latter dominates in the high latitudes, and the sedimentary ^{231}Pa decreases there by the bottom scavenging effect. The effect of bottom scavenging on ^{230}Th is also basically similar to ^{231}Pa .



370 4.2 Comparison with previous modeling studies

Additional insights on the simulated distribution of $^{231}\text{Pa}/^{230}\text{Th}$ ratios can be obtained from a comparison of CTRL_EXP with Siddall_EXP which uses the same model setting and parameter values in Siddall et al. (2005). Siddall_EXP (Fig. S4a) reproduces sedimentary $^{231}\text{Pa}/^{230}\text{Th}$ ratios as realistically as does CTRL_EXP (Fig. 6e), but the process determining the distribution is different from that in CTRL_EXP. Assuming the mass balance of ^{231}Pa and ^{230}Th are
375 in a steady state, we calculate the residence time of ^{231}Pa and ^{230}Th from the following formulas:

$$\tau^i = \int A_{\text{total}}^i dv / F_{\text{in}}^i, \quad (11a)$$

$$F_{\text{in}}^i = \int \beta^i dv, \quad (11b)$$

In Eq. (11a) and (11b), the integral domain is global and the parameters are described in Table 1. The residence times of ^{231}Pa and ^{230}Th are calculated to be 103 and 21 years, respectively, in CTRL_EXP, whereas they are 210 and 89 years,
380 respectively, in Siddall_EXP. By incorporating bottom scavenging and modifying the partition coefficient of ^{230}Th , the modeled residence time in CTRL_EXP comes close to the previous estimate based on data in Yu et al. (1996): 111 years for ^{231}Pa and 26 years for ^{230}Th . Because the reference partition coefficients for ^{231}Pa of Siddall_EXP and that of CTRL_EXP are the same value (i.e., $K_{\text{ref}}^{\text{Pa}} = 1.0 \times 10^7$), the influence of ocean transport on ^{231}Pa is identical in both experiments (Fig. 9a). Therefore, the difference in the ^{231}Pa distribution between the model experiments must come from the bottom scavenging,
385 which is included in CTRL_EXP but not in Siddall_EXP. The bottom scavenging reduces the residence time of ^{231}Pa in CTRL_EXP (103 years) compared to Siddall_EXP (210 years). The difference in the ^{230}Th distribution between CTRL_EXP and Siddall_EXP mainly comes from the difference in reference partition coefficients ($K_{\text{ref}}^{\text{Th}}$). The reference partition coefficient $K_{\text{ref}}^{\text{Th}}$ of CTRL_EXP, which depends on particle concentration, is larger than that of Siddall_EXP ($K_{\text{ref}}^{\text{Th}} = 6.0 \times 10^7$) in most of the ocean. Therefore, the contribution from the ocean transport of ^{230}Th becomes larger in Siddall_EXP (Fig. S4b)
390 than in CTRL_EXP (Fig. 6b). Together with additional contribution from the bottom scavenging effect on ^{230}Th (Fig. 9d), the residence time of ^{230}Th in CTRL_EXP (21 years) is shorter than that in Siddall_EXP (89 years). Since the residence time is overestimated for both ^{231}Pa and ^{230}Th in Siddall_EXP compared to CTRL_EXP, the distribution of sedimentary $^{231}\text{Pa}/^{230}\text{Th}$ ratios in Siddall_EXP ends up similar to that in CTRL_EXP. Our CTRL_EXP reproduces the distribution of sedimentary $^{231}\text{Pa}/^{230}\text{Th}$ ratios more realistically because our model can more realistically reproduce the dissolved ^{231}Pa and
395 ^{230}Th than in previous studies. Besides, the residence time of ^{231}Pa and ^{230}Th is also consistent with the observational estimate in Yu et al. (1996).

This study newly introduces a $^{231}\text{Pa}/^{230}\text{Th}$ model to the existing global three-dimensional OGCM. Based on the reversible scavenging model, this study well reproduces the distribution of dissolved concentration of ^{231}Pa and ^{230}Th by considering the bottom scavenging and the dependence of the scavenging efficiency on particle concentration. The
400 importance of bottom scavenging on the dissolved concentration of ^{231}Pa and ^{230}Th is already discussed in previous studies (Rempfer et al., 2017; Lerner et al., 2020). Therefore, our result should be viewed as a confirmation of these previous results



in this meaning. However, it is emphasized that this study provides a new estimate of this contribution to the distribution of sedimentary $^{231}\text{Pa}/^{230}\text{Th}$ ratios compared to other processes such as advection and water-column scavenging. Rempfer et al. (2017) evaluated the performance of their ^{231}Pa and ^{230}Th simulations based on the root mean squared deviation normalized by the standard deviation of observations. In our control experiment (CTRL_EXP), the RMSD between the available GEOTRACES data is 0.57 for dissolved ^{231}Pa and 0.51 for dissolved ^{230}Th . These values lie in the range of values for the “standard” and “optimal” experiments of Rempfer et al. (2017), the latter of which considers both bottom scavenging and boundary scavenging (see Fig. 5 in Rempfer et al., 2017). Lerner et al. (2020) use a regional eddy-permitting ocean circulation model and focus on the western North Atlantic. They also point out that removal in the nepheloid layer significantly impacts the basin-scale distribution of dissolved and particulate phases of ^{231}Pa and ^{230}Th . In line with these previous studies, our result confirmed the importance of the boundary scavenging. Recently, Gardner et al. (2018) reported data on the distribution of particles in benthic nepheloid layers. If such datasets become available for specifying the global distribution of particles in nepheloid layers, the effect of bottom scavenging can be introduced more realistically. It is also expected that additional consideration about boundary scavenging helps to improve our model simulation.

In addition to the bottom scavenging, our study highlights the importance of the dependence of scavenging efficiency on particle concentration. Although the decrease of the partition coefficient with increased bulk particle concentration has been reported from observations, the dependence of scavenging efficiency on particle concentration considered in PCE_EXP is not entirely understood (Honeyman et al. 1988; Henderson et al. 1999; Hayes et al. 2015). Recently, the particle concentration effect on ^{231}Pa and ^{230}Th partition coefficients in the open ocean along the GEOTRACES GA03 transect has been reported (Hayes et al., 2015; Lerner et al., 2017). Their study suggests that the dependency in the open ocean may deviate from Eq. (10). In discussing the factors responsible for the particle concentration effect, Pavia et al. (2018) point out the possibility that the particle concentration effect is an artifact caused by filtration. Further research is needed to elucidate the mechanisms that control the particle concentration effect.

As another remaining problem, as pointed out in previous studies (Rempfer et al., 2017; Lerner et al., 2020), it is not easy to reproduce the distribution of particle phase of these two radioisotopes than the dissolved phase. Part of the error comes from the oceanic flow fields simulated in the ocean model. It is also related to the particle fluxes that we give as an empirical distribution based on satellite observations. A $^{231}\text{Pa}/^{230}\text{Th}$ modeling study using an ecosystem model that considers six different particles well reproduce the distribution of ^{231}Pa and ^{230}Th with a simple reversible scavenging model (van Hulst et al., 2018). For dissolved ^{230}Th , the correlation coefficient between their model and observations is 0.80 for the GEOTRACES GA02 transect and 0.78 for the GA03 transect, comparable to our CTRL_EXP of 0.84 and 0.70, respectively. Furthermore, By examining the response of ^{231}Pa and ^{230}Th to freshwater forcing into the North Atlantic, Missiaen et al. (2020b) show that changes in biogenic particle fluxes may have caused 30% of the changes in the sedimentary $^{231}\text{Pa}/^{230}\text{Th}$ ratios during the Heinrich stadial 1. Therefore, the role of particle fields on the distribution of ^{231}Pa and ^{230}Th , which was not directly investigated in this study, needs to be further discussed in a future study.



435 5 Summary and concluding remarks

Previous modeling studies succeeded in reproducing the observed distribution of sedimentary $^{231}\text{Pa}/^{230}\text{Th}$ ratios but overestimated the dissolved concentration of ^{231}Pa and ^{230}Th in the deep ocean. To improve simulations of ^{231}Pa and ^{230}Th in the ocean, we performed OGCM experiments that incorporated the bottom scavenging and the dependence of scavenging efficiency on particle concentration together with the water-column reversible scavenging. Furthermore, we quantitatively
440 evaluated the processes that determine the global distribution of sedimentary $^{231}\text{Pa}/^{230}\text{Th}$ ratios, which is used as a proxy for the strength of paleo-ocean circulation.

First, we performed an OGCM experiment using the same model settings and parameters as Siddall et al. (2005) (Siddall_EXP), which reproduced the vertical profiles of dissolved ^{231}Pa and ^{230}Th similar to that reported in Siddall et al. (2005). In Siddall_EXP, the simulated concentrations of ^{231}Pa and ^{230}Th increase with depth, consistent with data; however,
445 this experiment significantly overestimated the concentrations observed in the deep ocean. To reduce this overestimation, we incorporated bottom scavenging in nepheloid layers following Rempfer et al. (2017) (BTM_EXP). We found that the overestimation of dissolved ^{231}Pa and ^{230}Th is reduced in this case, as reported in Rempfer et al. (2017). In BTM_EXP, we successfully reproduced the observed vertical profile of dissolved ^{231}Pa . However, this experiment had difficulty in reproducing the observed vertical profile of dissolved ^{230}Th . Therefore, we modified the parameters associated with the
450 strength of water-column scavenging (i.e., K_{ref} : the reference partition coefficient for sinking particles) with the consideration of the bottom scavenging (KREF_EXP). When we increased the reference partition coefficient of ^{230}Th ($K_{\text{ref}}^{\text{Th}} = 6.0 \times 10^7$) from that used in the Siddall_EXP with the consideration of bottom scavenging ($K_{\text{bottom}}^{\text{Th}} = 1.0 \times 10^7$), dissolved ^{230}Th was found to be more realistically simulated. However, the concentration of dissolved ^{230}Th is still significantly underestimated in the Southern Ocean. This underestimation can be improved when we further considered the
455 dependence of K_{ref} on particle concentration following Henderson et al. (1999) (PCE_EXP). This study shows that our OGCM simulation considering the reversible scavenging, bottom scavenging, and the dependence of scavenging efficiency on particle concentration (CTRL_EXP) can most successfully reproduce the observed distributions of dissolved ^{231}Pa and ^{230}Th and sedimentary $^{231}\text{Pa}/^{230}\text{Th}$ ratios.

We then quantitatively assessed the processes that determine the global distribution of sedimentary $^{231}\text{Pa}/^{230}\text{Th}$
460 ratios. For our best simulation (CTRL_EXP), we decomposed the processes affecting the sediment $^{231}\text{Pa}/^{230}\text{Th}$ ratios into three parts: water-column scavenging, ocean transport, and bottom scavenging. For this decomposition, we perform additional sensitivity simulations (1D_EXP and 3D_EXP) to evaluate how these three processes control the distribution of sedimentary $^{231}\text{Pa}/^{230}\text{Th}$ ratios. We found that the global sedimentary $^{231}\text{Pa}/^{230}\text{Th}$ ratios in our model are primarily determined by ocean transport of ^{231}Pa , as in previous models. Contrary to ^{231}Pa , ocean transport of ^{230}Th tends to reduce the spatial
465 contrast of sedimentary $^{231}\text{Pa}/^{230}\text{Th}$ ratios. However, we found that this is not the case for the Southern Ocean; ^{230}Th advection increases the sedimentary $^{231}\text{Pa}/^{230}\text{Th}$ ratios in the Southern Ocean and strengthens the observed high $^{231}\text{Pa}/^{230}\text{Th}$ ratios there. In other words, not only ^{231}Pa advection but also ^{230}Th advection contributes to the high $^{231}\text{Pa}/^{230}\text{Th}$ ratios in the



Southern Ocean. This result implies that scavenging of ^{230}Th is not much efficient in the Southern Ocean as conventionally thought when we consider the dependence of scavenging efficiency on particle concentration. We also show that bottom scavenging works opposite to ocean transport and decreases the spatial contrast of $^{231}\text{Pa}/^{230}\text{Th}$ ratios; bottom scavenging promotes the removal of ^{231}Pa near the sea bottom more efficiently than that of ^{230}Th , and the total effect of bottom scavenging reduces spatial contrasts of the $^{231}\text{Pa}/^{230}\text{Th}$ ratios.

Finally, we compared experiments CTRL_EXP and Siddall_EXP; both experiments well reproduce the distribution of sedimentary $^{231}\text{Pa}/^{230}\text{Th}$ ratios, but it is clarified that the contributions from the three processes above, water-column scavenging, ocean transport, and the bottom scavenging, are different between these two experiments. We show the similarity of Siddall_EXP to CTRL_EXP about sedimentary $^{231}\text{Pa}/^{230}\text{Th}$ ratios is caused by the offsetting influences of the ocean transports of ^{231}Pa and ^{230}Th . In CTRL_EXP, the ocean residence time of ^{231}Pa and ^{230}Th (103 and 21 years) is close to the previous estimate (Yu et al., 1996; 111 and 26 years), whereas the residence time of ^{231}Pa and ^{230}Th are both overestimated in Siddall_EXP (210 and 89 years). Our model successfully reproduces the global distribution of the sedimentary $^{231}\text{Pa}/^{230}\text{Th}$ ratios with the realistic residence time of ^{231}Pa and ^{230}Th . In contrast, previous models that reported sedimentary $^{231}\text{Pa}/^{230}\text{Th}$ ratios similar to ours are shown to significantly overestimate the residence times for both ^{231}Pa and ^{230}Th .

The model developed in this study is useful not only for simulating $^{231}\text{Pa}/^{230}\text{Th}$ ratios in the present-day ocean but also in different climates such as glacial periods. Our OGCM experiments using the present-day physical fields can clarify the processes governing the global distribution of sedimentary $^{231}\text{Pa}/^{230}\text{Th}$ ratios by decomposing patterns into three components: water-column scavenging, ocean transport, and bottom scavenging. A similar analysis using the physical ocean fields during glacial periods may help climate scientists to understand the mechanisms for glacial changes in the sedimentary $^{231}\text{Pa}/^{230}\text{Th}$ ratio observed in sediment cores. Simulation of $^{231}\text{Pa}/^{230}\text{Th}$ ratios under glacial climates (e.g., Oka et al., 2011; Kobayashi and Oka, 2018) is an exciting avenue of future study.

490 Code and data availability

The $^{231}\text{Pa}/^{230}\text{Th}$ model code and data used to produce the results in this study are available at the repository website Zenodo: <https://doi.org/10.5281/zenodo.4600287> (Sasaki et al., 2021a) and <https://doi.org/10.5281/zenodo.4655882> (Sasaki et al., 2021b), respectively. COCO is an ocean component of MIROC and the code of COCO4 is included as a part of MIROC-ES2L. The source code of MIROC-ES2L can be obtained from <https://doi.org/10.5281/zenodo.3893386> (Ohgaito et al., 2020).

Supplement

The supplement related to this article is available online at: <https://doi.org/xxxx>.



Author contributions

500 Y.S. and A.O. contributed to the interpretation of the simulation results. Y.S. performed the numerical simulations. A.O. designed and supervised the study. Y.S. and H.K. analyzed the results. Y.S. wrote the first draft and the final draft was prepared with the inputs from all the coauthors.

Competing interests

The authors declare that they have no conflict of interest.

Acknowledgments

505 The authors acknowledge many constructive comments from reviewers, which significantly improves the manuscript. This work was supported by JSPS KAKENHI Grant Number JP19H01963.

References

- Anderson, R. F., Bacon, M. P., and Brewer, P. G.: Removal of ^{230}Th and ^{231}Pa from the open ocean, *Earth Planet. Sci. Lett.*, *62*(1), 7–23, [https://doi.org/10.1016/0012-821X\(83\)90067-5](https://doi.org/10.1016/0012-821X(83)90067-5), 1983.
- 510 Bacon, M. P., and Anderson, R. F.: Distribution of thorium isotopes between dissolved and particulate forms in the deep sea, *J. Geophys. Res.*, *87*(C3), 2045, <https://doi.org/10.1029/JC087iC03p02045>, 1982.
- Behrenfeld, M. J., and Falkowski, P. G.: Photosynthetic rates derived from satellite-based chlorophyll concentration, *Limnol. Oceanogr.*, *42*(1), 1–20, <https://doi.org/10.4319/lo.1997.42.1.0001>, 1997.
- 515 Böhm, E., Lippold, J., Gutjahr, M., Frank, M., Blaser, P., Antz, B., Fohlmeister, J., Frank, N., Anderson, M. B., and Deininger, M.: Strong and deep Atlantic meridional overturning circulation during the last glacial cycle, *Nature*, *517*(7532), 73–76, <https://doi.org/10.1038/nature14059>, 2015.
- Bradt Miller, L. I., McManus, J. F., and Robinson, L. F.: $^{231}\text{Pa}/^{230}\text{Th}$ evidence for a weakened but persistent Atlantic meridional overturning circulation during Heinrich Stadial 1, *Nat. Commun.*, *5*(1), 5817, <https://doi.org/10.1038/ncomms6817>, 2014.
- 520 Chase, Z., and Anderson, R. F.: Comment on “On the importance of opal, carbonate, and lithogenic clays in scavenging and fractionating ^{230}Th , ^{231}Pa and ^{10}Be in the ocean” by S. Luo and T.-L. Ku., *Earth Planet. Sci. Lett.*, *220*(1–2), 213–222, [https://doi.org/10.1016/S0012-821X\(04\)00028-7](https://doi.org/10.1016/S0012-821X(04)00028-7), 2004.
- Chase, Z., Anderson, R. F., Fleisher, M. Q., and Kubik, P. W.: The influence of particle composition and particle flux on scavenging of Th, Pa and Be in the ocean, *Earth Planet. Sci. Lett.*, *204*(1–2), 215–229, [https://doi.org/10.1016/S0012-](https://doi.org/10.1016/S0012-821X(02)00984-6)
- 525 [821X\(02\)00984-6](https://doi.org/10.1016/S0012-821X(02)00984-6), 2002.



- Chase, Z., Anderson, R. F., Fleisher, M. Q., and Kubik, P. W.: Scavenging of ^{230}Th , ^{231}Pa and ^{10}Be in the Southern Ocean (SW Pacific sector): the importance of particle flux, particle composition and advection, *Deep-Sea Res. II*, 50(3–4), 739–768, [https://doi.org/10.1016/S0967-0645\(02\)00593-3](https://doi.org/10.1016/S0967-0645(02)00593-3), 2003.
- 530 Cochran, J. K., Livingston, H. D., Hirschberg, D. J., and Surprenant, L. D.: Natural and anthropogenic radionuclide distributions in the northwest Atlantic Ocean, *Earth Planet. Sci. Lett.*, 84(2–3), 135–152, [https://doi.org/10.1016/0012-821X\(87\)90081-1](https://doi.org/10.1016/0012-821X(87)90081-1), 1987.
- Colley, S., Thomson, J., and Newton, P. P.: Detailed ^{230}Th , ^{232}Th and ^{210}Pb fluxes recorded by the 1989/90 BOFS sediment trap time-series at 48°N , 20°W , *Deep-Sea Res. I*, 42(6), 833–848, [https://doi.org/10.1016/0967-0637\(95\)00033-3](https://doi.org/10.1016/0967-0637(95)00033-3), 1995.
- 535 Deng F., Henderson, G. M., Castrillejo, M., Perez, F. F., and Steinfeldt, R.: Evolution of ^{231}Pa and ^{230}Th in overflow waters of the North Atlantic, *Biogeosciences*, 15, 7299–7313, <https://doi.org/10.5194/bg-15-7299-2018>, 2018.
- Dunne, J. P., Armstrong, R. A., Gnanadesikan, A., and Sarmiento, J. L.: Empirical and mechanistic models for the particle export ratio, *Glob. Biogeochem. Cycles*, 19(4), <https://doi.org/10.1029/2004GB002390>, 2005.
- 540 Dutay, J.-C., Lacan, F., Roy-Barman, M., and Bopp, L.: Influence of particle size and type on ^{231}Pa and ^{230}Th simulation with a global coupled biogeochemical-ocean general circulation model: A first approach, *Geochem. Geophys. Geosyst.*, 10, Q01011, <https://doi.org/10.1029/2008GC002291>, 2009.
- Edwards, N. R., Stocker, T. F., Joos, F., Henderson, G. M., Frank, M., Siddall, M., and Müller, S. A.: $^{231}\text{Pa}/^{230}\text{Th}$ fractionation by ocean transport, biogenic particle flux and particle type, *Earth Planet. Sci. Lett.*, 237(1–2), 135–155, <https://doi.org/10.1016/j.epsl.2005.05.031>, 2005.
- 545 François, R., Bacon, M. P., Altabet, M. A., and Labeyrie, L. D.: Glacial/interglacial changes in sediment rain rate in the SW Indian Sector of subantarctic Waters as recorded by ^{230}Th , ^{231}Pa , U, and $\delta^{15}\text{N}$, *Paleoceanography*, 8(5), 611–629, <https://doi.org/10.1029/93PA00784>, 1993.
- 550 Frank, M., Eckhardt, J.-D., Eisenhauer, A., Kubik, P. W., Dittrich-Hannen, B., Segl, M., and Mangini, A.: Beryllium 10, thorium 230, and protactinium 231 in Galapagos microplate sediments: Implications of hydrothermal activity and paleoproductivity changes during the last 100,000 years, *Paleoceanography*, 9(4), 559–578, <https://doi.org/10.1029/94PA01132>, 1994.
- Gardner, W. D., Mishonov, A. V., and Richardson, M. J.: Decadal Comparisons of Particulate Matter in Repeat Transects in the Atlantic, Pacific, and Indian Ocean Basins, *Geophys. Res. Lett.*, 45(1), 277–286, <https://doi.org/10.1002/2017GL076571>, 2018.
- 555 Gherardi, J.-M., Labeyrie, L., Nave, S., François, R., McManus, J. F., and Cortijo, E.: Glacial-interglacial circulation changes inferred from $^{231}\text{Pa}/^{230}\text{Th}$ sedimentary record in the North Atlantic region, *Paleoceanography*, 24(2), PA2204, <https://doi.org/10.1029/2008PA001696>, 2009.
- Gregory, J. M., Dixon, K. W., Stouffer, R. J., Weaver, A. J., Driesschaert, E., Eby, M., Fichefet, T., Hasumi, H., Hu, A., Jungclaus, J. H., Kamenkovich, I. V., Levermann, A., Montoya, M., Murakami, S., Nawrath, S. Oka, A., Sokolov, A.



- 560 P., Thorpe, R. B.: A model intercomparison of changes in the Atlantic thermohaline circulation in response to increasing atmospheric CO₂ concentration, *Geophys. Res. Lett.*, 32(12), 1–5, <https://doi.org/10.1029/2005GL023209>, 2005.
- Gu, S., and Liu, Z.: 231Pa and 230Th in the ocean model of the Community Earth System Model (CESM1.3), *Geosci. Model Dev.*, 10, 4723–4742, <https://doi.org/10.5194/gmd-10-4723-2017>, 2017.
- 565 Guo, L., Santschi, P. H., Baskaran, M., and Zindler, A.: Distribution of dissolved and particulate 230Th and 232Th in seawater from the Gulf of Mexico and off Cape Hatteras as measured by SIMS, *Earth Planet. Sci. Lett.*, 133(1–2), 117–128, [https://doi.org/10.1016/0012-821X\(95\)00063-I](https://doi.org/10.1016/0012-821X(95)00063-I), 1995.
- Hajima, T., Watanabe, M., Yamamoto, A., Tatebe, H., Noguchi, M. A., Abe, M., Ohgaito, R., Ito, A., Yamazaki, D., Okajima, H., Ito, A., Takata, K., Ogochi, K., Watanabe, S., and Kawamiya, M.: Development of the MIROC-ES2L
570 Earth system model and the evaluation of biogeochemical processes and feedbacks, *Geosci. Model Dev.*, 13, 2197–2244, <https://doi.org/10.5194/gmd-13-2197-2020>, 2020.
- Hasumi, H.: CCSR Ocean Component Model (COCO) version 4.0. *CCSR Rep. 25*, 103 pp., Center for Climate System Research, Univ. of Tokyo, 2006.
- Hayes, C. T., Anderson, R. F., Jaccard, S. L., François, R., Fleisher, M. Q., Soon, M., Gersonde, R.: A new perspective on
575 boundary scavenging in the North Pacific Ocean, *Earth Planet. Sci. Lett.*, 369–370, 86–97. <https://doi.org/10.1016/j.epsl.2013.03.008>, 2013.
- Hayes, C. T., Anderson, R. F., Fleisher, M. Q., Huang, K.-F., Robinson, L. F., Lu, Y., Cheng, H., Lawrence Edwards, R., and Bradley Moran, S.: 230Th and 231Pa on GEOTRACES GA03, the U.S. GEOTRACES North Atlantic transect, and implications for modern and paleoceanographic chemical fluxes, *Deep-Sea Res. II.*, 116, 29–41,
580 <https://doi.org/10.1016/j.dsr2.2014.07.007>, 2015.
- Henderson, G. M., and Anderson, R. F.: The U-series Toolbox for Paleooceanography. *Reviews in Mineralogy and Geochemistry*, 52(1), 493–531, <https://doi.org/10.2113/0520493>, 2003.
- Henderson, Gideon M., Heinze, C., Anderson, R. F., and Winguth, A. M. E.: Global distribution of the 230Th flux to ocean sediments constrained by GCM modeling, *Deep-Sea Res. I.*, 46(11), 1861–1893, [https://doi.org/10.1016/S0967-0637\(99\)00030-8](https://doi.org/10.1016/S0967-0637(99)00030-8), 1999.
585
- Honeyman, B. D., Balistrieri, L. S., and Murray, J. W.: Oceanic trace metal scavenging: the importance of particle concentration, *Deep-Sea Res. A.*, 35(2), 227–246, [https://doi.org/10.1016/0198-0149\(88\)90038-6](https://doi.org/10.1016/0198-0149(88)90038-6), 1988.
- Honjo, S., Manganini, S. J., Krishfield, R. A., and François, R.: Particulate organic carbon fluxes to the ocean interior and factors controlling the biological pump: A synthesis of global sediment trap programs since 1983, *Prog. Oceanogr.*,
590 76(3), 217–285, <https://doi.org/10.1016/j.pocean.2007.11.003>, 2008.
- K-1 Model Developers: K-1 coupled GCM (MIROC) description. In H. Hasumi, & S. Emori (Eds.), *K-1 Tech. Rep. 1*, 34 pp., Center for Climate System Research, Univ. of Tokyo, 2004.



- Kobayashi, H., Abe-Ouchi, A., and Oka, A.: Role of Southern Ocean stratification in glacial atmospheric CO₂ reduction evaluated by a three-dimensional ocean general circulation model, *Paleoceanography*, 30(9), 1202–1216, 595 <https://doi.org/10.1002/2015PA002786>, 2015.
- Kobayashi, H., and Oka, A.: Response of atmospheric pCO₂ to glacial changes in the Southern Ocean amplified by carbonate compensation, *Paleoceanogr. Paleoclimatol.*, 33(11), 1206–1229, <https://doi.org/10.1029/2018PA003360>, 2018.
- Lam, P. J., Ohnemus, D. C., and Auro, M. E.: Size-fractionated major particle composition and concentrations from the US 600 GEOTRACES North Atlantic Zonal Transect, *Deep-Sea Res. II: Topical Studies in Oceanography*, 116, 303–320, <https://doi.org/10.1016/J.DSR2.2014.11.020>, 2015.
- Lerner P., Marchal O., Lam P., Buesseler K., Charette M.: Kinetics of thorium and particle cycling along the U.S. GEOTRACES North Atlantic transect, *Deep-Sea Research I*, 125, 106–128, <https://doi.org/10.1016/j.dsr.2017.05.003>, 2017.
- 605 Lerner, P., Marchal, O., Lam, P. J., Gardner, W., Richardson, M. J., and Mishonov, A.: A model study of the relative influences of scavenging and circulation on ²³⁰Th and ²³¹Pa in the western North Atlantic, *Deep-Sea Res. I*, 155, 103159, <https://doi.org/10.1016/j.dsr.2019.103159>, 2020.
- Luo, S., and Ku, T. L.: Oceanic ²³¹Pa/²³⁰Th ratio influenced by particle composition and remineralization, *Earth Planet. Sci. Lett.*, 167(3–4), 183–195, [https://doi.org/10.1016/S0012-821X\(99\)00035-7](https://doi.org/10.1016/S0012-821X(99)00035-7), 1999.
- 610 Luo, Y., François, R., and Allen, S. E.: Sediment ²³¹Pa/²³⁰Th as a recorder of the rate of the Atlantic meridional overturning circulation: Insights from a 2-D model, *Ocean Sci.*, 6(1), 381–400, <https://doi.org/10.5194/os-6-381-2010>, 2010.
- Maier-Reimer, E.: Geochemical cycles in an ocean general circulation model. Preindustrial tracer distributions, *Glob. Biogeochem. Cycles*, 7(3), 645–677, <https://doi.org/10.1029/93GB01355>, 1993.
- 615 Mangini, A., and Sonntag, C.: ²³¹Pa dating of deep-sea cores via ²²⁷Th counting, *Earth Planet. Sci. Lett.*, 37(2), 251–256, [https://doi.org/10.1016/0012-821X\(77\)90170-4](https://doi.org/10.1016/0012-821X(77)90170-4), 1977.
- Marchal, O., François, R., Stocker, T. F., and Joos, F.: Ocean thermohaline circulation and sedimentary ²³¹Pa/²³⁰Th ratio, *Paleoceanography*, 15(6), 625–641, <https://doi.org/10.1029/2000PA000496>, 2000.
- Marchal, O., Stocker, T. F., and Joos, F.: A latitude-depth, circulation-biogeochemical ocean model for paleoclimate studies. 620 Development and sensitivities, *Tellus B*, 50(3), 290–316, <https://doi.org/10.3402/tellusb.v50i3.16130>, 1998.
- McManus, J. F., François, R., Gherardl, J. M., Kelgwin, L., and Drown-Leger, S.: Collapse and rapid resumption of Atlantic meridional circulation linked to deglacial climate changes, *Nature*, 428(6985), 834–837, <https://doi.org/10.1038/nature02494>, 2004.
- Missiaen, L., Bouttes, N., Roche, D. M., Dutay, J.-C., Quiquet, A., Waelbroeck, C., Pichat, S., Peterschmitt, J.-Y.: Carbon 625 isotopes and Pa/Th response to forced circulation changes: a model perspective, *Clim. Past*, 16(3), 867–883, <https://doi.org/10.5194/cp-16-867-2020>, 2020a



- Missiaen, L., Menviel, L. C., Meissner, K. J., Roche, D. M., Dutay, J.-C., Bouttes, N., Lhardy, F., Quiquet, A., Pichat, S., Waelbroeck, C.: Modelling the impact of biogenic particle flux intensity and composition on sedimentary Pa/Th, *Quaternary Sci. Rev.*, 240, 106394, <https://doi.org/10.1016/j.quascirev.2020.106394>, 2020b.
- 630 Moran, S. B., Charette, M. A., Hoff, J. A., Edwards, R. L., and Landing, W. M.: Distribution of ^{230}Th in the Labrador Sea and its relation to ventilation, *Earth Planet. Sci. Lett.*, 150(1–2), 151–160, [https://doi.org/10.1016/s0012-821x\(97\)00081-2](https://doi.org/10.1016/s0012-821x(97)00081-2), 1997.
- Moran, S. B., Shen, C. C., Edmonds, H. N., Weinstein, S. E., Smith, J. N., and Edwards, R. L.: Dissolved and particulate ^{231}Pa and ^{230}Th in the Atlantic Ocean: Constraints on intermediate/deep water age, boundary scavenging, and $^{231}\text{Pa}/^{230}\text{Th}$ fractionation, *Earth Planet. Sci. Lett.*, 203(3–4), 999–1014, [https://doi.org/10.1016/S0012-821X\(02\)00928-7](https://doi.org/10.1016/S0012-821X(02)00928-7), 2002.
- 635 Moran, S. B., Shen, C.-C., Weinstein, S. E., Hettlinger, L. H., Hoff, J. H., Edmonds, H. N., and Edwards, R. L.: Constraints on deep water age and particle flux in the equatorial and South Atlantic Ocean based on seawater ^{231}Pa and ^{230}Th data, *Geophys. Res. Lett.*, 28(18), 3437–3440, <https://doi.org/10.1029/2001GL013339>, 2001.
- 640 Müller, P. J., and Mangini, A.: Organic carbon decomposition rates in sediments of the Pacific manganese nodule belt dated by ^{230}Th and ^{231}Pa , *Earth Planet. Sci. Lett.*, 51(1), 94–114, [https://doi.org/10.1016/0012-821X\(80\)90259-9](https://doi.org/10.1016/0012-821X(80)90259-9), 1980.
- Oka, A., Hasumi, H., and Abe-Ouchi, A.: The thermal threshold of the Atlantic meridional overturning circulation and its control by wind stress forcing during glacial climate, *Geophys. Res. Lett.*, 39(9), <https://doi.org/10.1029/2012GL051421>, 2012.
- 645 Oka, A., Hasumi, H., Obata, H., Gamo, T., and Yamanaka, Y.: Study on vertical profiles of rare earth elements by using an ocean general circulation model, *Glob. Biogeochem. Cycles*, 23(4), GB4025, <https://doi.org/10.1029/2008GB003353>, 2009.
- Oka, A., Hasumi, H., Okada, N., Sakamoto, T. T., and Suzuki, T.: Deep convection seesaw controlled by freshwater transport through the Denmark Strait, *Ocean Model.*, 15(3–4), 157–176, <https://doi.org/10.1016/j.ocemod.2006.08.004>, 2006.
- 650 Oka, A., Kato S., and Hasumi H.: Evaluating effect of ballast mineral on deep-ocean nutrient concentration by using an ocean general circulation model, *Glob. Biogeochem. Cycles*, 22(3), <https://doi.org/10.1029/2007GB003067>, 2008.
- Oka, A., Tazoe H., and Obata, H.: Simulation of global distribution of rare earth elements in the ocean using an ocean general circulation model, *Journal of Oceanography*, <https://doi.org/10.1007/s10872-021-00600-x>, 2021.
- Okubo, A., Obata, H., Gamo, T., and Yamada, M.: ^{230}Th and ^{232}Th distributions in mid-latitudes of the North Pacific Ocean: Effect of bottom scavenging, *Earth Planet. Sci. Lett.*, 339–340, 139–150, <https://doi.org/10.1016/J.EPSL.2012.05.012>, 2012.
- 655 Ohgaito, R., Yamamoto, A., Hajima, T., Oishi, R., Abe, M., Tatebe, H., Abe-Ouchi, A., and Kawamiya, M.: Core code of MIROC-ES2L, Geoscientific Model Development, Zenodo, <https://doi.org/10.5281/zenodo.3893386>, 2020.



- Ohgaito, R., Yamamoto, A., Hajima, T., O'ishi, R., Abe, M., Tatebe, H., Abe-Ouchi, A., and Kawamiya, M.: PMIP4
660 experiments using MIROC-ES2L Earth system model, *Geosci. Model Dev.*, 14, 1195–1217,
<https://doi.org/10.5194/gmd-14-1195-2021>, 2021.
- Pavia, F., Anderson, R., Vivancos, S., Fleisher, M., Lam, P., Lu, Y., Cheng, H., Zhang, P., Lawrence Edwards, R.: Intense
hydrothermal scavenging of ^{230}Th and ^{231}Pa in the deep Southeast Pacific, *Mar. Chem.*, 201, 212–228,
<https://doi.org/10.1016/J.MARCHEM.2017.08.003>, 2018.
- 665 Rempfer, J., Stocker, T. F., Joos, F., Lippold, J., and Jaccard, S. L.: New insights into cycling of ^{231}Pa and ^{230}Th in the
Atlantic Ocean, *Earth Planet. Sci. Lett.*, 468, 27–37, <https://doi.org/10.1016/j.epsl.2017.03.027>, 2017.
- Roy-Barman, M.: Modeling the effect of boundary scavenging on Thorium and Protactinium profiles in the ocean.
Biogeosciences, 6(12), 3091–3107, <https://doi.org/10.5194/bg-6-3091-2009>, 2009.
- Rutgers van der Loeff, M. M., and Berger, G. W.: Scavenging of ^{230}Th and ^{231}Pa near the antarctic polar front in the South
670 Atlantic, *Deep-Sea Res. I*, 40(2), 339–357, [https://doi.org/10.1016/0967-0637\(93\)90007-P](https://doi.org/10.1016/0967-0637(93)90007-P), 1993.
- Sasaki, Y., Kobayashi, H., A. Oka : Data for the figures of Sasaki et al. entitled "An investigation into the processes
controlling the global distribution of dissolved ^{231}Pa and ^{230}Th in the ocean and the sedimentary $^{231}\text{Pa}/^{230}\text{Th}$ ratios
by using an ocean general circulation model COCO ver4.0.", <https://doi.org/10.5281/zenodo.4600287>, 2021a.
- Sasaki, Y., Kobayashi, H., A. Oka : Code of Sasaki et al. entitled "An investigation into the processes controlling the global
675 distribution of dissolved ^{231}Pa and ^{230}Th in the ocean and the sedimentary $^{231}\text{Pa}/^{230}\text{Th}$ ratios by using an ocean
general circulation model COCO ver4.0.", <https://doi.org/10.5281/zenodo.4600287>, 2021b.
- Schlitzer, R., Anderson, R. F., Dodas, E. M., Lohan, M., Geibert, W., Tagliabue, A., Bowie, A., Jeandel, C., Maldonado, M.
T., Landing, W. M., Cockwell, D. et al.: The GEOTRACES Intermediate Data Product 2017, *Chem. Geol.*, 493, 210–
223, <https://doi.org/10.1016/j.chemgeo.2018.05.040>, 2018.
- 680 Schmitz, W., Mangini, A., Stoffers, P., Glasby, G. P., and Plüger, W. L.: Sediment accumulation rates in the southwestern
Pacific Basin and Aitutaki Passage, *Mar. Geol.*, 73(1–2), 181–190, [https://doi.org/10.1016/0025-3227\(86\)90118-0](https://doi.org/10.1016/0025-3227(86)90118-0),
1986.
- Shimmield, G. B., Murray, J. W., Thomson, J., Bacon, M. P., Anderson, R. F., and Price, N. B.: The distribution and
behaviour of ^{230}Th and ^{231}Pa at an ocean margin, Baja California, Mexico, *Geochim. Cosmochim. Acta*, 50(11),
685 2499–2507, [https://doi.org/10.1016/0016-7037\(86\)90032-3](https://doi.org/10.1016/0016-7037(86)90032-3), 1986.
- Shimmield, G. B., and Price, N. B.: The scavenging of U, ^{230}Th and ^{231}Pa during pulsed hydrothermal activity at 20°S ,
East Pacific Rise, *Geochim. Cosmochim. Acta*, 52(3), 669–677, [https://doi.org/10.1016/0016-7037\(88\)90329-8](https://doi.org/10.1016/0016-7037(88)90329-8), 1988.
- Siddall, M., Henderson, G. M., Edwards, N. R., Frank, M., Mu, S. A., Stocker, T. F., and Joos, F.: $^{231}\text{Pa}/^{230}\text{Th}$
fractionation by ocean transport, biogenic particle flux and particle type, *Earth Planet. Sci. Lett.*, 237, 135–155,
690 <https://doi.org/10.1016/j.epsl.2005.05.031>, 2005.
- Stouffer, R. J., Yin, J., Gregory, J. M., Dixon, K. W., Spelman, M. J., Hurlin, W., Weaver, A. J., Eby, M., Flato, G. M.,
Hasumi, H., Hu, A., Jungclaus, J. H., Kamenkovich, I. V., Levermann, A., Montoya, M., Murakami, S., Nawrath, S.,



- 695 Oka, A., Peltier, W. R., Robitaille, D. Y., Sokolov, A., Vettoretti, G., Weber, S. L.: Investigating the Causes of the Response of the Thermohaline Circulation to Past and Future Climate Changes, *J. Climate*, 19(8), 1365–1387, <https://doi.org/10.1175/JCLI3689.1>, 2006.
- Yang, H.-S., Nozaki, Y., Sakai, H., and Masuda, A.: The distribution of ^{230}Th and ^{231}Pa in the deep-sea surface sediments of the Pacific Ocean, *Geochim. Cosmochim. Acta*, 50(1), 81–89, [https://doi.org/10.1016/0016-7037\(86\)90050-5](https://doi.org/10.1016/0016-7037(86)90050-5), 1986.
- van Hulst, M., Dutay, J.-C., and Roy-Barman, M.: A global scavenging and circulation ocean model of thorium-230 and protactinium-231 with improved particle dynamics (NEMO-ProThorP 0.1), *Geosci. Model Dev.*, 11, 3537–3556, <https://doi.org/10.5194/gmd-11-3537-2018>, 2018.
- 700 Vogler, S., Scholten, J., Rutgers Van Der Loeff, M., and Mangini, A.: ^{230}Th in the eastern North Atlantic: The importance of water mass ventilation in the balance of ^{230}Th , *Earth Planet. Sci. Lett.*, 156(1–2), 61–74, [https://doi.org/10.1016/s0012-821x\(98\)00011-9](https://doi.org/10.1016/s0012-821x(98)00011-9), 1998.
- Walter, H. J., Rutgers Van Der Loeff, M. M., and Hoeltzen, H.: Enhanced scavenging of ^{231}Pa relative to ^{230}Th in the South Atlantic south of the Polar Front: Implications for the use of the $^{231}\text{Pa}/^{230}\text{Th}$ ratio as a paleoproductivity proxy, *Earth Planet. Sci. Lett.*, 149(1–4), 85–100, [https://doi.org/10.1016/s0012-821x\(97\)00068-x](https://doi.org/10.1016/s0012-821x(97)00068-x), 1997.
- 705 Yong Lao, Anderson, R. F., Broecker, W. S., Trumbore, S. E., Hofmann, H. J., and Wolfli, W.: Transport and burial rates of ^{10}Be and ^{231}Pa in the Pacific Ocean during the Holocene period, *Earth Planet. Sci. Lett.*, 113(1–2), [https://doi.org/10.1016/0012-821X\(92\)90218-K](https://doi.org/10.1016/0012-821X(92)90218-K), 1992.
- 710 Yu, E.-F., François, R., and Bacon, M. P.: Similar rates of modern and last-glacial ocean thermohaline circulation inferred from radiochemical data, *Nature*, 379(6567), 689–694, <https://doi.org/10.1038/379689a0>, 1996.

Figure 1. (a) Dissolved ^{231}Pa along 30°W in the Atlantic Ocean and (b) its vertical profile averaged horizontally along 30°W in Siddall_EXP. (c, d) Same as Figs. 1a and 1b except for ^{230}Th . The colored circles in Figs. 1a and 1c represent data from the Atlantic GEOTRACES data (GA02 and GIPY05; Schlitzer et al., 2018). The green and orange circles in Figs. 1b and 1d represent the GA02 data and simulation results.

715

Figure 2. (a, c, e) Dissolved ^{231}Pa along 30°W in the Atlantic Ocean and (b, d, f) its vertical profile averaged horizontally along 30°W in BTM_EXP. $K_{\text{bottom}}^{\text{Pa}}$ is set to 5.0×10^4 in Figs. 2a and 2b, 5.0×10^5 in Figs. 2c and 2d, and 5.0×10^6 in Figs. 2e and 2f. The colored circles in Figs. 2a, 2c, and 2e represent data from the Atlantic GEOTRACES data (GA02 and GIPY05; Schlitzer et al., 2018). The green and orange circles in Figs. 2b, 2d, and 2f represent the GA02 data and simulation results.

720

Figure 3. (a, c, e, g) Dissolved ^{230}Th along 30°W in the Atlantic Ocean and (b, d, f, h) its vertical profile averaged horizontally along 30°W in BTM_EXP are plotted. $K_{\text{bottom}}^{\text{Th}}$ is set to 5.0×10^5 in Figs. 3a and 3b, 1.0×10^6 in Figs. 3c and 3d, 5.0×10^6 in Figs. 3e and 3f, and 1.0×10^7 in Figs. 3g and 3h. The colored circles in Figs. 3a, 3c, 3e, and 3g represent data from the Atlantic GEOTRACES data (GA02 and GIPY05; Schlitzer et al., 2018). The green and orange circles in Figs. 3b, 3d, 3f, and 3h represent the GA02 data and simulation results.

725



Figure 4. The vertical profile of dissolved ^{230}Th averaged horizontally along 30°W in various simulations of KREF_EXP: (a) R2_B20, (b) R2_B10, (c) R2_B5, (d) R4_B10, (e) R4_B5, and (f) R6_B5. The green and orange circles in Figs. 4a–4f represent the Atlantic GEOTRACES data (GA02; Schlitzer et al., 2018) and simulation results. Figure 4g summarizes the choice of parameters (i.e., $K_{\text{ref}}^{\text{Th}}$ and $K_{\text{bottom}}^{\text{Th}}$) in each simulation.

Figure 5. Dissolved ^{230}Th along 30°W in the Atlantic Ocean in (a) R6_B5 of the KREF_EXP and (b) PCE_EXP. (c) Reference coefficient (K_{ref}) along 30°W in the Atlantic Ocean in PCE_EXP. (d) The vertical profile of dissolved ^{230}Th averaged horizontally along 30°W in R6_B5 of KREF_EXP and PCE_EXP. The colored circles in Figs. 5a and 5b represent data from the Atlantic GEOTRACES data (GA02 and GIPY05; Schlitzer et al., 2018). The green, yellow, and orange circles in Fig. 5d represent the GA02 data and KREF_EXP and PCE_EXP simulation results.

Figure 6. (a) Dissolved ^{231}Pa , (b) dissolved ^{230}Th , (c) particulate ^{231}Pa , and (d) particulate ^{230}Th along 30°W in the Atlantic Ocean in CTRL_EXP. (e) Sedimentary $^{231}\text{Pa}/^{230}\text{Th}$ ratios normalized by the production ratio of 0.093 in CTRL_EXP. The colored circles represent observational data. Dissolved ^{231}Pa and ^{230}Th data are taken from the Atlantic GEOTRACES data (GA02 and GIPY05; Schlitzer et al., 2018). Particulate ^{231}Pa and ^{230}Th data are taken from the following references (Colley et al., 1995; Moran et al., 1997; Moran et al., 2001; Rutgers van der Loeff and Berger, 1993; Vogler et al., 1998; Walter et al., 1997; Cochran et al., 1987; Moran et al., 2002; Guo et al., 1995). The data of sedimentary $^{231}\text{Pa}/^{230}\text{Th}$ ratios are taken from the following references (Mangianini & Sonntag, 1977; Muller & Mangini, 1980; Anderson et al., 1983; Shimmield et al., 1986; Schmitz et al., 1986; Yang et al., 1986; Shimmield & Price, 1988; Yong Lao et al., 1992; François et al., 1993; Frank et al., 1994; Frank, 1996; Bradtmiller et al., 2014, Luo et al., 2010, and their supplemental data).

Figure 7. The difference between 3D_EXP and 1D_EXP (i.e., 3D_EXP minus 1D_EXP, which represents for ocean transport effect) of (a) dissolved ^{231}Pa , (b) dissolved ^{230}Th , (c) particulate ^{231}Pa , and (d) particulate ^{230}Th along 30°W in the Atlantic Ocean. (e) The difference between 3D_EXP and 1D_EXP of sedimentary $^{231}\text{Pa}/^{230}\text{Th}$ ratios normalized by the production ratio of 0.093.

Figure 8. The difference between CTRL_EXP and 3D_EXP (i.e., CTRL_EXP minus 3D_EXP, which represents for bottom scavenging effect) of (a) dissolved ^{231}Pa , (b) dissolved ^{230}Th , (c) particulate ^{231}Pa , and (d) particulate ^{230}Th along 30°W in the Atlantic Ocean. (e) The difference between CTRL_EXP and 3D_EXP of the sedimentary $^{231}\text{Pa}/^{230}\text{Th}$ ratios normalized by the production ratio of 0.093.

Figure 9. Sedimentary $^{231}\text{Pa}/^{230}\text{Th}$ ratios normalized by the production ratio of 0.093 in CTRL_EXP decomposed into contributions from (a) ocean transport solely from ^{231}Pa (i.e., $^{231}\text{Pa}(3\text{D})/^{230}\text{Th}(1\text{D})$), (b) ocean transport solely from ^{230}Th (i.e., $^{231}\text{Pa}(1\text{D})/^{230}\text{Th}(3\text{D})$), (c) bottom scavenging solely from ^{231}Pa (i.e., $^{231}\text{Pa}(\text{CTRL})/^{230}\text{Th}(3\text{D})$ minus $^{231}\text{Pa}(3\text{D})/^{230}\text{Th}(3\text{D})$), and (d) bottom scavenging solely from ^{230}Th (i.e., $^{231}\text{Pa}(3\text{D})/^{230}\text{Th}(\text{CTRL})$ minus $^{231}\text{Pa}(3\text{D})/^{230}\text{Th}(3\text{D})$).

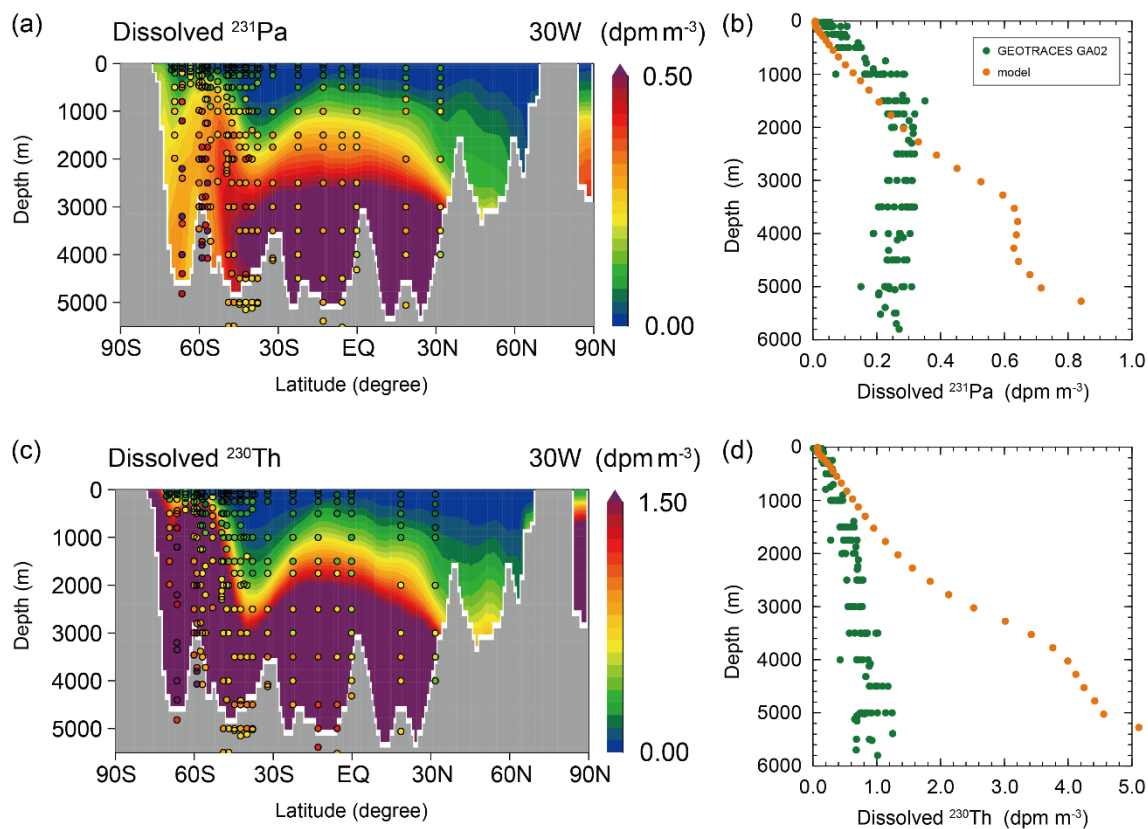
760

Table 1. Parameters of the ^{231}Pa and ^{230}Th model.

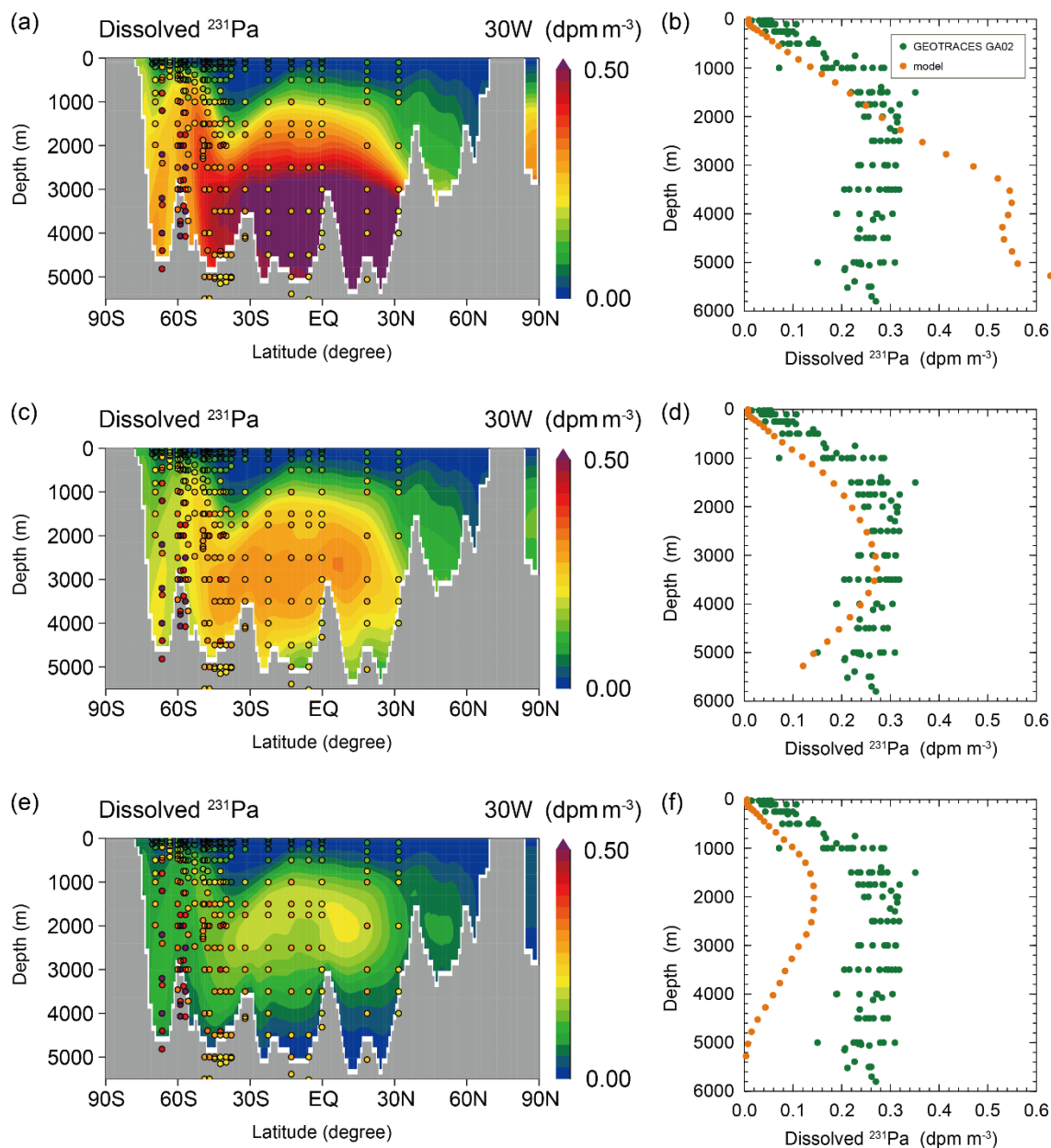
Table 2. Equilibrium partition coefficients in experiments Siddall_EXP and CTRL_EXP.



765 **Table 3.** Processes considered in additional experiments. A circle means that the process is considered, and a cross means that it is not considered.



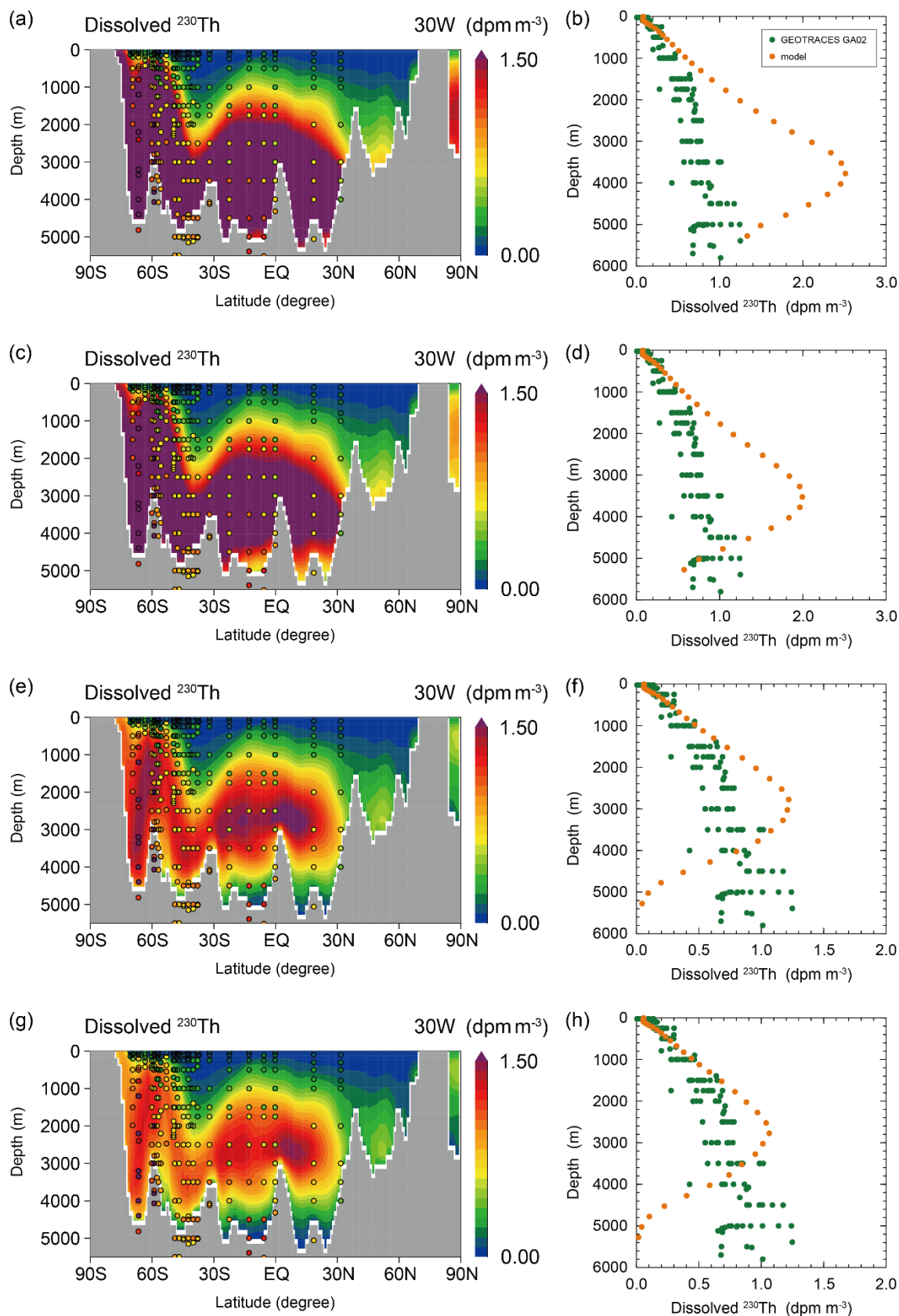
770 Figure 1. (a) Dissolved ^{231}Pa along 30°W in the Atlantic Ocean and (b) its vertical profile averaged horizontally along 30°W in Siddall_EXP. (c, d) Same as Figs. 1a and 1b except for ^{230}Th . The colored circles in Figs. 1a and 1c represent data from the Atlantic GEOTRACES data (GA02 and GIPY05; Schlitzer et al., 2018). The green and orange circles in Figs. 1b and 1d represent the GA02 data and simulation results.



775

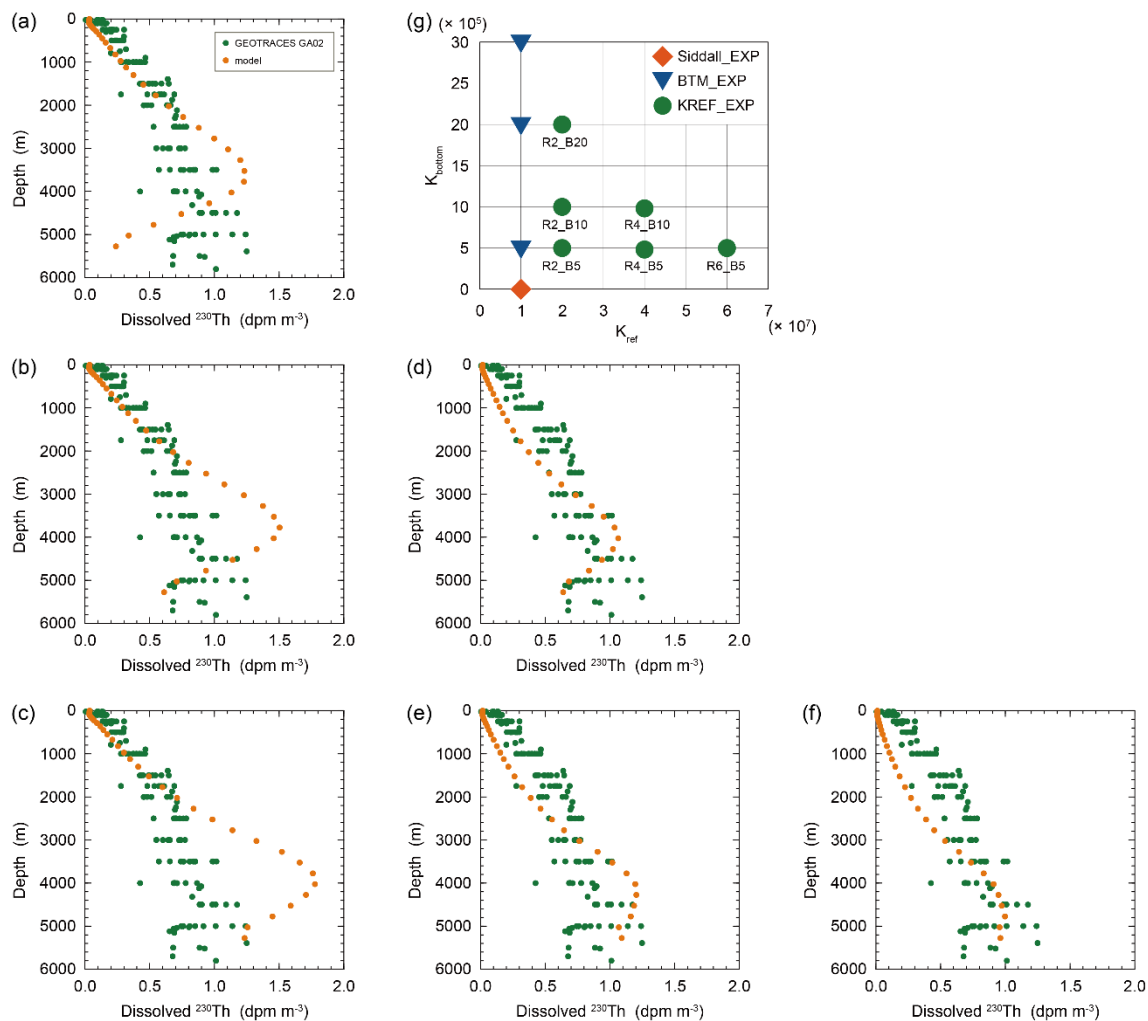
Figure 2. (a, c, e) Dissolved ^{231}Pa along 30°W in the Atlantic Ocean and (b, d, f) its vertical profile averaged horizontally along 30°W in BTM_EXP. $K_{\text{bottom}}^{\text{Pa}}$ is set to 5.0×10^4 in Figs. 2a and 2b, 5.0×10^5 in Figs. 2c and 2d, and 5.0×10^6 in Figs. 2e and 2f. The colored circles in Figs. 2a, 2c, and 2e represent data from the Atlantic GEOTRACES data (GA02 and GIPY05; Schlitzer et al., 2018). The green and orange circles in Figs. 2b, 2d, and 2f represent the GA02 data and simulation results.

780





785 Figure 3. (a, c, e, g) Dissolved ^{230}Th along 30°W in the Atlantic Ocean and (b, d, f, h) its vertical profile averaged horizontally along 30°W in BTM_EXP are plotted. $K_{\text{bottom}}^{\text{Th}}$ is set to 5.0×10^5 in Figs. 3a and 3b, 1.0×10^6 in Figs. 3c and 3d, 5.0×10^6 in Figs. 3e and 3f, and 1.0×10^7 in Figs. 3g and 3h. The colored circles in Figs. 3a, 3c, 3e, and 3g represent data from the Atlantic GEOTRACES data (GA02 and GIPY05; Schlitzer et al., 2018). The green and orange circles in Figs. 3b, 3d, 3f, and 3h represent the GA02 data and simulation results.



790

Figure 4. The vertical profile of dissolved ^{230}Th averaged horizontally along 30°W in various simulations of KREF_EXP: (a) R2_B20, (b) R2_B10, (c) R2_B5, (d) R4_B10, (e) R4_B5, and (f) R6_B5. The green and orange circles in Figs. 4a–4f represent the Atlantic GEOTRACES data (GA02; Schlitzer et al., 2018) and simulation results. Figure 4g summarizes the choice of parameters (i.e., $K_{\text{ref}}^{\text{Th}}$ and $K_{\text{bottom}}^{\text{Th}}$) in each simulation.

795

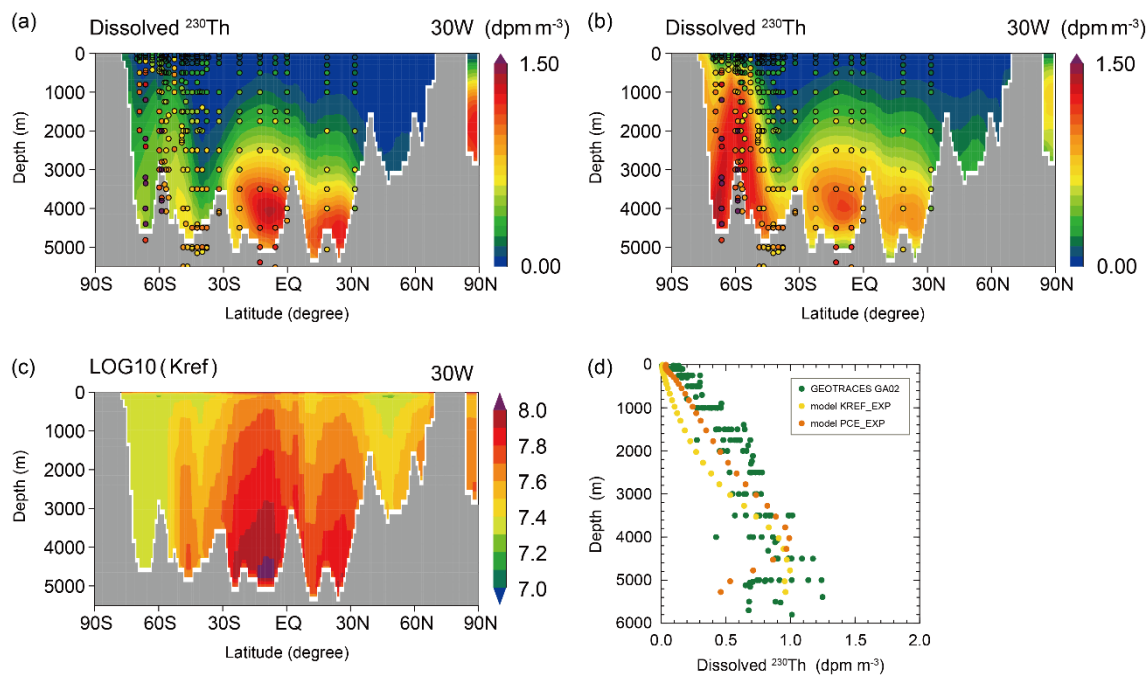
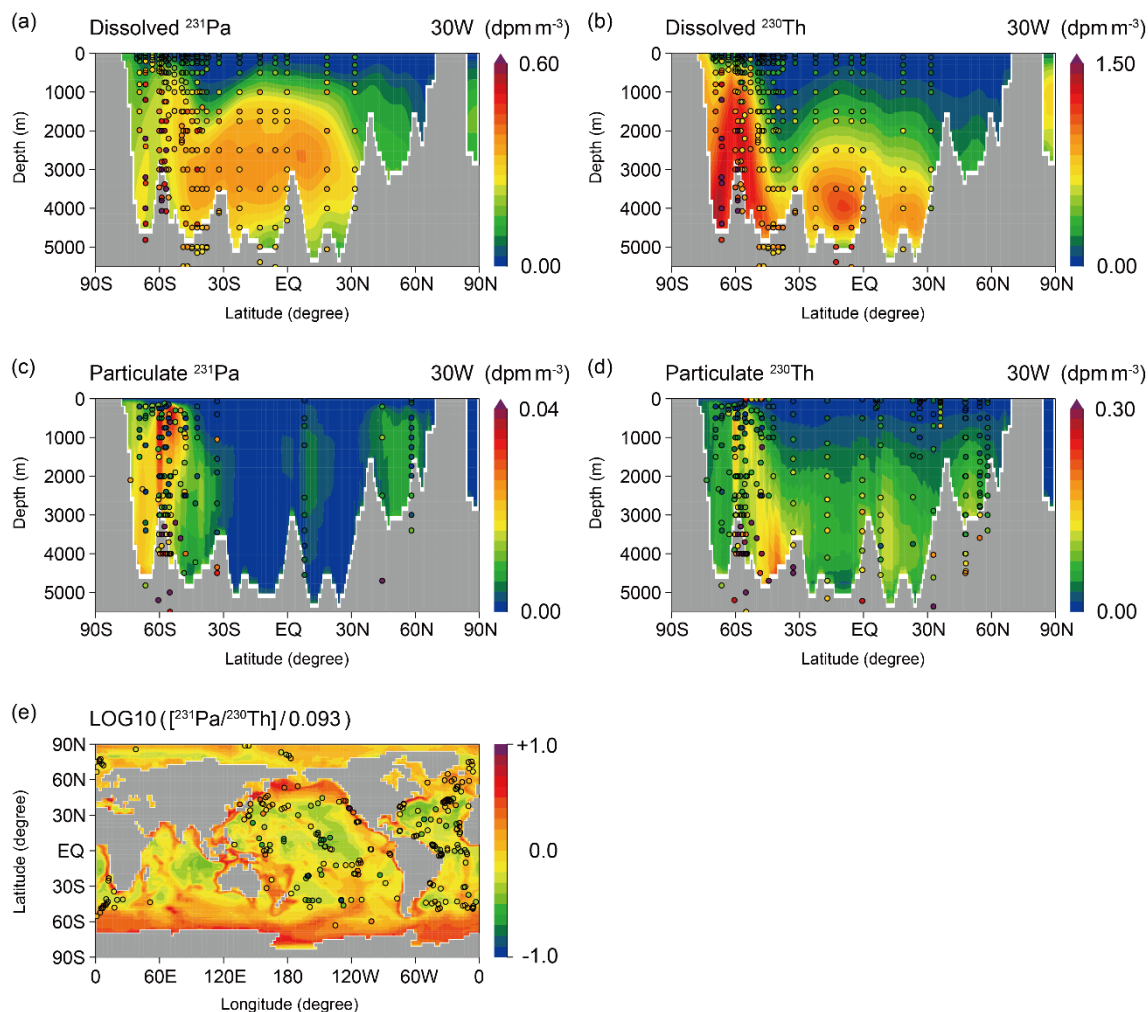


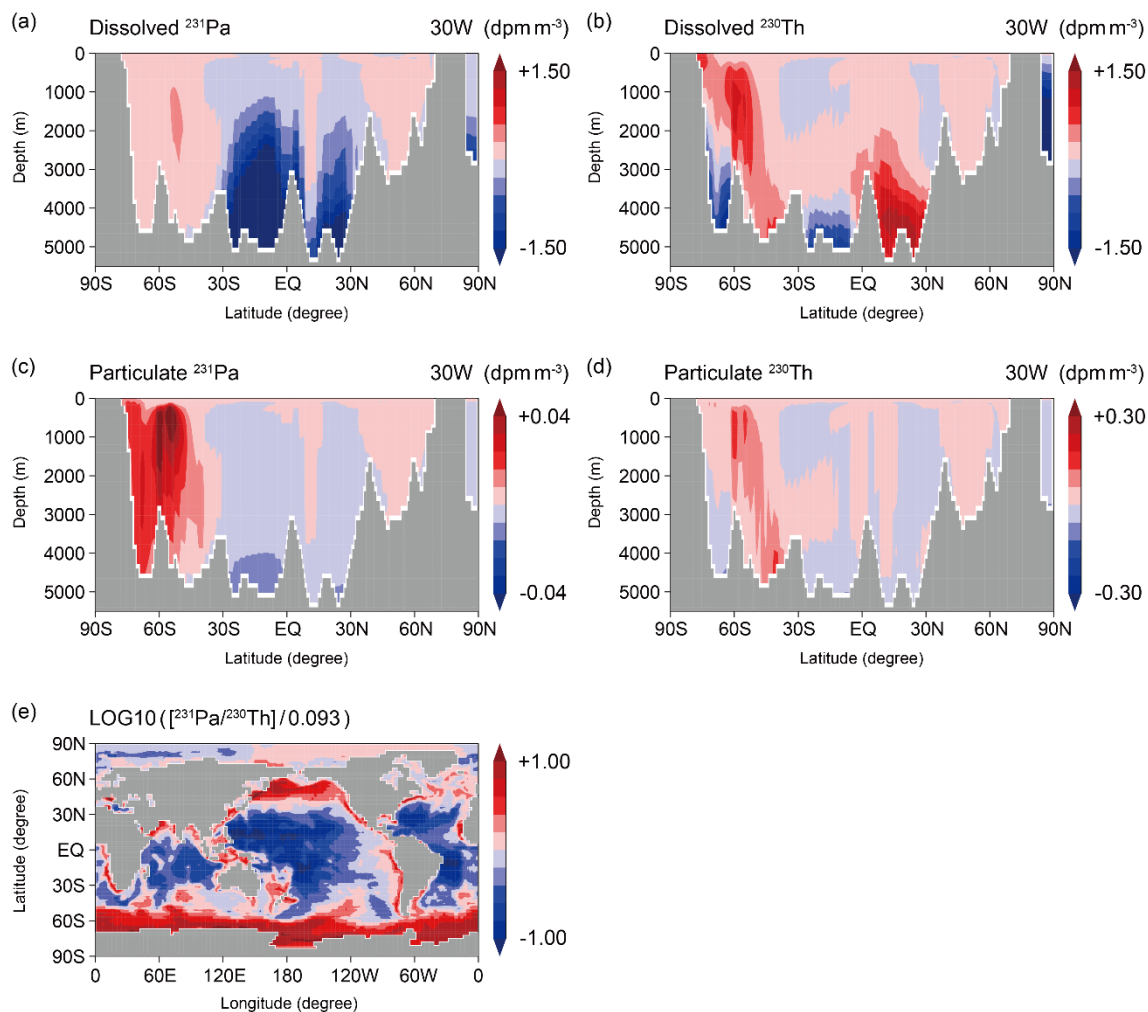
Figure 5. Dissolved ^{230}Th along 30°W in the Atlantic Ocean in (a) R6_B5 of the KREF_EXP and (b) PCE_EXP. (c) Reference coefficient (K_{ref}) along 30°W in the Atlantic Ocean in PCE_EXP. (d) The vertical profile of dissolved ^{230}Th averaged horizontally along 30°W in R6_B5 of KREF_EXP and PCE_EXP. The colored circles in Figs. 5a and 5b represent data from the Atlantic GEOTRACES data (GA02 and GIPY05; Schlitzer et al., 2018). The green, yellow, and orange circles in Fig. 5d represent the GA02 data and KREF_EXP and PCE_EXP simulation results.



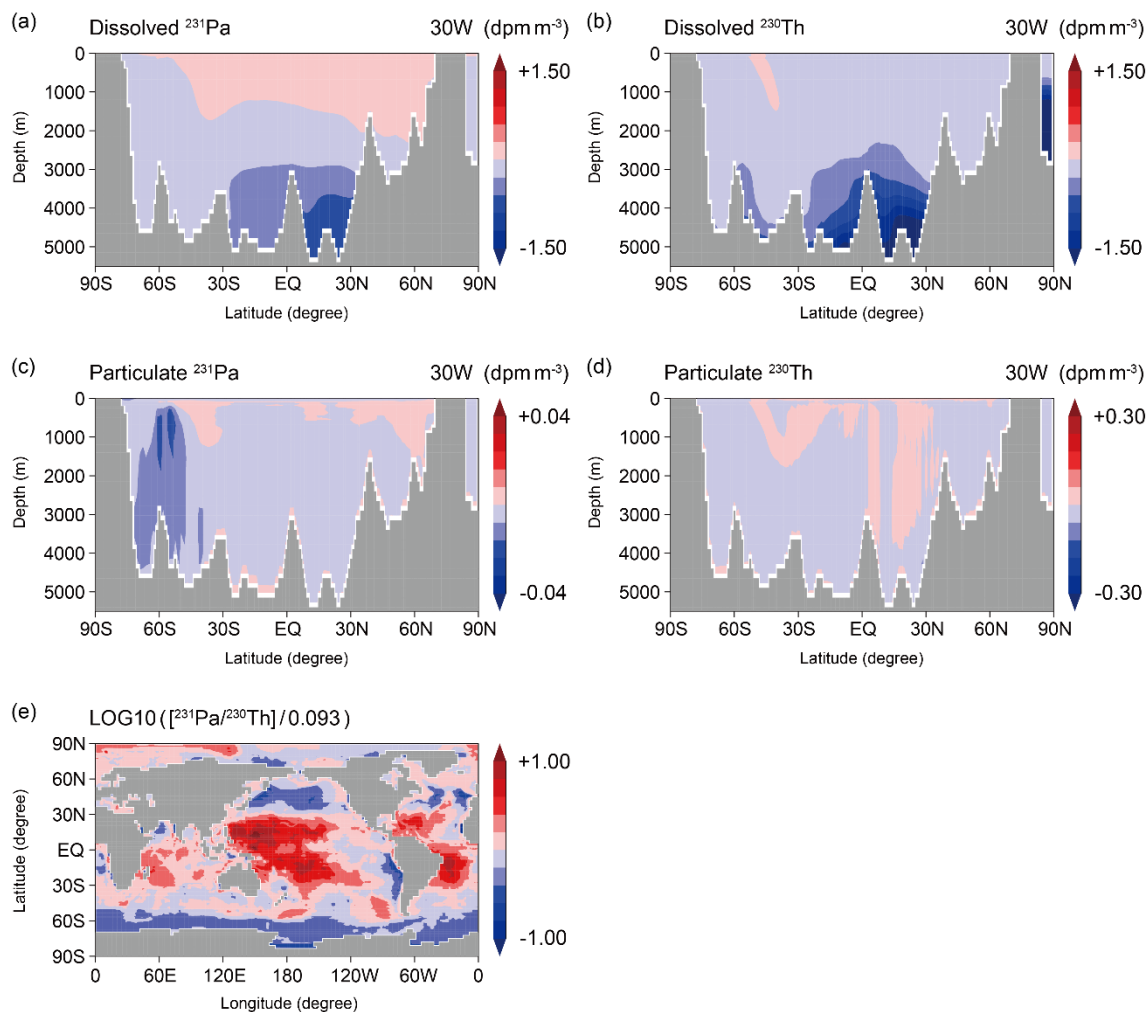
805

Figure 6. (a) Dissolved ^{231}Pa , (b) dissolved ^{230}Th , (c) particulate ^{231}Pa , and (d) particulate ^{230}Th along 30°W in the Atlantic Ocean in CTRL_EXP. (e) Sedimentary $^{231}\text{Pa}/^{230}\text{Th}$ ratios normalized by the production ratio of 0.093 in CTRL_EXP. The colored circles represent observational data. Dissolved ^{231}Pa and ^{230}Th data are taken from the Atlantic GEOTRACES data (GA02 and GIPY05; Schlitzer et al., 2018). Particulate ^{231}Pa and ^{230}Th data are taken from the following references (Colley et al., 1995; Moran et al., 1997; Moran et al., 2001; Rutgers van der Loeff and Berger, 1993; Vogler et al., 1998; Walter et al., 1997; Cochran et al., 1987; Moran et al., 2002; Guo et al., 1995). The data of sedimentary $^{231}\text{Pa}/^{230}\text{Th}$ ratios are taken from the following references (Mangianini & Sonntag, 1977; Muller & Mangini, 1980; Anderson et al., 1983; Shimmield et al., 1986; Schmitz et al., 1986; Yang et al., 1986; Shimmield & Price, 1988; Yong Lao et al., 1992; François et al., 1993; Frank et al., 1994; Frank, 1996; Bradtmiller et al., 2014, Luo et al., 2010, and their supplemental data).

815



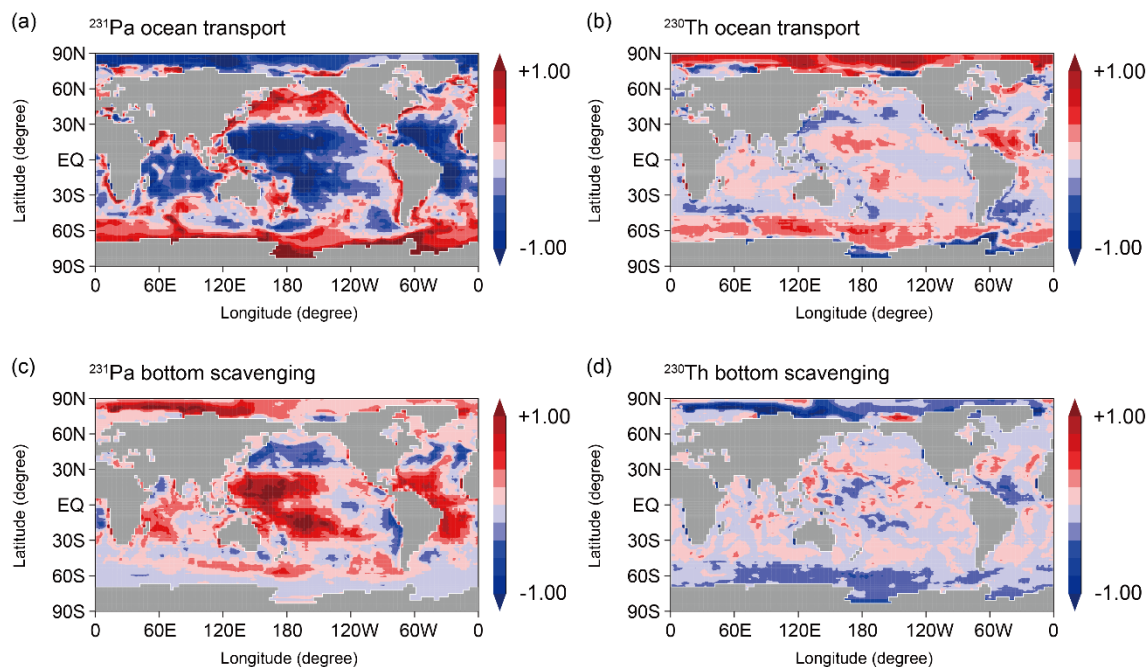
820 Figure 7. The difference between 3D_EXP and 1D_EXP (i.e., 3D_EXP minus 1D_EXP, which represents for ocean transport effect) of (a) dissolved ^{231}Pa , (b) dissolved ^{230}Th , (c) particulate ^{231}Pa , and (d) particulate ^{230}Th along 30°W in the Atlantic Ocean. (e) The difference between 3D_EXP and 1D_EXP of sedimentary $^{231}\text{Pa}/^{230}\text{Th}$ ratios normalized by the production ratio of 0.093.



825

Figure 8. The difference between CTRL_EXP and 3D_EXP (i.e., CTRL_EXP minus 3D_EXP, which represents for bottom scavenging effect) of (a) dissolved ^{231}Pa , (b) dissolved ^{230}Th , (c) particulate ^{231}Pa , and (d) particulate ^{230}Th along 30°W in the Atlantic Ocean. (e) The difference between CTRL_EXP and 3D_EXP of the sedimentary $^{231}\text{Pa}/^{230}\text{Th}$ ratios normalized by the production ratio of 0.093.

830



835 Figure 9. Sedimentary $^{231}\text{Pa}/^{230}\text{Th}$ ratios normalized by the production ratio of 0.093 in CTRL_EXP decomposed into contributions from (a) ocean transport solely from ^{231}Pa (i.e., $^{231}\text{Pa}(3\text{D})/^{230}\text{Th}(1\text{D})$), (b) ocean transport solely from ^{230}Th (i.e., $^{231}\text{Pa}(1\text{D})/^{230}\text{Th}(3\text{D})$), (c) bottom scavenging solely from ^{231}Pa (i.e., $^{231}\text{Pa}(\text{CTRL})/^{230}\text{Th}(3\text{D})$ minus $^{231}\text{Pa}(3\text{D})/^{230}\text{Th}(3\text{D})$), and (d) bottom scavenging solely from ^{230}Th (i.e., $^{231}\text{Pa}(3\text{D})/^{230}\text{Th}(\text{CTRL})$ minus $^{231}\text{Pa}(3\text{D})/^{230}\text{Th}(3\text{D})$).



Variable	Symbol	Value	Units
^{231}Pa production from ^{235}U decay	β^{Pa}	2.33×10^{-3}	$\text{dpm m}^{-3} \text{ yr}^{-1}$
^{230}Th production from ^{234}U decay	β^{Th}	2.52×10^{-2}	$\text{dpm m}^{-3} \text{ yr}^{-1}$
Decay constant of ^{231}Pa	λ^{Pa}	2.13×10^{-5}	yr^{-1}
Decay constant of ^{230}Th	λ^{Th}	9.12×10^{-6}	yr^{-1}
Sinking velocity of particles	w_s	1000	m yr^{-1}
Thickness of euphotic zone	z_0	100	m
Penetration depth of CaCO_3	z_p	2000	m
Dissolution constant of opal	B	0.12	$^{\circ}\text{C}^{-1} \text{ yr}^{-1}$
Minimum temperature of sea water	T_0	-2	$^{\circ}\text{C}$
Dissolution rate of POC	ε	0.858	-
Total activity of ^{231}Pa or ^{230}Th	A_{total}	variable	dpm m^{-3}
Activity of dissolved ^{231}Pa or ^{230}Th	A_d	variable	dpm m^{-3}
Activity of particle ^{231}Pa or ^{230}Th	A_p	variable	dpm m^{-3}
Ratio of particle concentration to fluid density	C	variable	-

840

Table 1. Parameters of the ^{231}Pa and ^{230}Th model.



Experiment	Siddall_EXP		CTRL_EXP	
	^{231}Pa	^{230}Th	^{231}Pa	^{230}Th
K_{ref}	1.0×10^7	1.0×10^7	1.0×10^7	$\left(\frac{C_{\text{total}}}{10^{-7}}\right)^{-0.42} \times 10^7$
K_{CaCO_3}	$K_{\text{ref}} / 40$	K_{ref}	$K_{\text{ref}} / 40$	K_{ref}
K_{opal}	$K_{\text{ref}} / 6$	$K_{\text{ref}} / 20$	$K_{\text{ref}} / 6$	$K_{\text{ref}} / 20$
K_{POC}	K_{ref}	K_{ref}	K_{ref}	K_{ref}
K_{bottom}	0	0	5.0×10^5	5.0×10^5

Table 2. Equilibrium partition coefficients in experiments Siddall_EXP and CTRL_EXP.



Experiment	Water-column reversible scavenging	Bottom scavenging	Ocean transport
CTRL_EXP	0	0	0
3D_EXP	0	X	0
1D_EXP	0	X	X

Table 3. Processes considered in additional experiments. A circle means that the process is considered, and a cross means that it is not considered.